NUMERICAL SIMULATION OF VORTEX-INDUCED VIBRATIONS OF FREE SPAN PIPELINES INCLUDING NONLINEAR SOIL MODELS

A Thesis

by

YIFEI ZHU

Submitted to the Office of Graduate and Professional Studies of
Texas A&M University
in partial fulfillment of the requirements for the degree of

MASTER OF SCIENCE

Chair of Committee,	Hamn-Ching Chen
Committee Members,	Richard Mercier
	Andrew Comech
Head of Department,	Sharath Girimaji

August 2017

Major Subject: Ocean Engineering

ABSTRACT

This thesis introduces a fully three dimensional (3D) numerical simulation method of the VIV behaviors of free span pipelines by considering the nonlinear pipe-soil interaction effect. The pipeline is modeled as a tensioned beam of which the governing equations are numerically solved by applying a fully implicit discretization scheme. Reynolds Averaged Navier-Stokes (RANS) equations are numerically solved to compute the fluid domain. An overset grid method is utilized in discretizing the fluid field around the pipeline. Six computational blocks and nearly 1 million grid points are needed in the simulation. It is a good strategy to generate finer grid in the near body regions and relatively coarse grid in the far field. By exchanging motions and forces between the pipeline motion solver and the fluid solver, fluid-structure interaction is achieved. This research also includes a nonlinear soil model to simulate the pipe-soil interaction which is considered as a spring-pipeline system while the stiffness characteristics are expressed by using a nonlinear force-displacement (*P-y*) curves.

The simulation results are compared with model tests or other numerical simulations for validation in two cases: (1) a free span pipeline of *G/D*=2.0 at different reduced velocities including linear and nonlinear soil models; (2) a free span pipeline of different *G/D* which ranges from 1.2 to 3.0.

DEDICATION

This thesis is dedicated to my girlfriend Iris Wu. Her encouragement and understanding have always been with me from the beginning of the research.

Also, this thesis is dedicated to my parents who supported me both mentally and financially.

ACKNOWLEDGEMENTS

I would like to thank my committee chair, Dr. Chen, my committee members, Dr. Mercier and Dr. Comech, for their support and guidance throughout the long journey of this research.

I would also thank my friends and the department faculty and staff for making my study experience at Texas A&M University a period of wonderful time. Thanks also go to the Texas A&M University Supercomputer Center, which provided the necessary facilities for my research work.

CONTRIBUTORS AND FUNDING SOURCES

This work was supervised by a thesis committee consisting of Professor Hamn-Ching Chen and Professor Richard Mercier of the Department of Civil Engineering and Professor Andrew Comech of the Department of Mathematics.

All work for the thesis was completed independently by the student.

There are no outside funding contributions to acknowledge related to the research and compilation of this document.

NOMENCLATURE

2D	Two Dimensional
3D	Three Dimensional
a	Backbone Curve Coefficient
b	Backbone Curve Exponent
c	Soil Strength
A_z	Cross Flow Vibration Amplitude
CFD	Computational Fluid Dynamics
C_L	Horizontal Dynamic Stiffness Factor
C_V	Vertical Dynamic Stiffness Factor
D	Pipeline Outer Diameter
D_s	Pipeline Damping
E	Young's Modulus
EI	Bending stiffness
f_n	Natural Frequency
F	External Force Matrix
FANS	Finite-Analytic Navier-Stokes
FSI	Fluid-Structure Interaction
G	Gap Depth

G/D	Gap to Diameter Ratio
I	Moment of Inertia
k_o/c	Unload Initial Stiffness
KC	Keulegan-Carpenter Number
K_L	Soil Horizontal Dynamic Stiffness
K_V	Soil Vertical Dynamic Stiffness
L	Pipeline Overall Length
L_s	Pipeline Span Length
LES	Large Eddy Simulation
M	Pipeline Unit Mass
N_p	Bearing Factor
P	Soil Resistance Force
RANS	Reynolds-Averaged Navier-Stokes
RMS	Root Mean Square
t	Time
T	Pipeline Axial Tension
U	Velocity of Current
VIV	Vortex-Induced Vibration
V_R	Reduced Velocity
W	Pipeline Weight Per Unit Length
X	Beam Displacement Matrix

y	In-Line Pipeline Displacement
z	Cross-Flow Pipeline Displacement
α	Current Flow Velocity Ratio
v	Poisson's Ratio
ρ_s/ρ	Pipeline to Water Density Ratio
ω	Unload Large Deflections
ϕ	Unload Tension Limit
ψ	Soil-Riser Separation
χ	Sign Mark

TABLE OF CONTENTS

Page

LIST OF FIGURES

Page

LIST OF TABLES

Page

CHAPTER I

INTRODUCTION AND LITERATURE REVIEW

In the fields of offshore oil and gas transportation, pipelines are widely used. While the most parts of the whole pipeline are supported by the seabed, some parts of it may become unsupported due to seabed unevenness, change of seabed topology, artificial supports, rock berms and strudel scours etc. This phenomenon is called free span (DNV, 2006). As currents pass by, the boundary layer flow around the pipelines separates and initiates vortex shedding which may cause vortex-induced vibrations (VIV) and finally could result in fatigue damage of the structures. Thus, predictions of VIV amplitude and frequency of free span pipelines are very important during the pipeline design process.

In the past several decades, offshore VIV problems were investigated based on many experimental studies. Pantazopoulos (1994) reviewed and evaluated more than 150 model tests of VIV phenomena in slender marine structures such as tethers and risers. Recommendations were provided for developing an empirical methodology for modeling hydrodynamic VIV behavior. Triantafyllou et al. (1999) developed a pragmatic VIV analysis methodology based on riser specific experimental tests and correlation length measurements to establish basic drag coefficients and lift coefficients databases for realistic riser configurations with buoyancy modules and auxiliary lines. Wilde and Huijsmans (2004) researched the 3D response of a long riser in currents by model tests of a circular steel pipe of 12.6 m long and 16 mm diameter. Different

responses under varying current speeds and with different pretensions were observed. Tognarelli et al. (2008) presented the findings from collected data of actual fatigue response of real dimension drilling riser VIV tests in the Gulf of Mexico and finally discovered some performance indicators for most widely used VIV suppression devices.

Due to the high speed development of super computational techniques, numerical simulations of VIV are more and more important nowadays. Researchers have considered it as a valuable alternative of experiments. Meneghini et al. (2003) investigated the hydro-elastic interactions between fluid forces and long oscillating flexible cylinders. Constantinides et al. (2006) utilized a second order accurate finite element computational fluid dynamics (CFD) method to numerically simulate both bare and straked cylinder VIV behavior. In addition, two turbulence models: the Detached Eddy Simulation (DES) and the Reynolds Averaged Navier Stokes (RANS) are compared in their paper. Huang et al. (2012) conducted a numerical simulation of a vertical riser VIV under sheared currents and compared the results with published experimental data. About 1.5 million elements were generated to simulate both the riser and the fluid domain outside. It is concluded that the CFD approach presented in the paper can predict the vertical riser VIV under sheared currents and the induced fatigue damage in an acceptable accuracy.

Specifically, VIV of free span pipelines has been studied by several researchers. Pontaza et al. (2010) investigated a pipeline which departs from the seabed and attaches to a pipeline end termination (PLET). A finite element model and CFD codes were coupled in the paper. The results revealed that the former design guidelines based on

VIV responses for isolated pipes will lead to overly conservative designs. Tsukada and Morooka (2013) used a nonlinear Finite Element Method (FEM) to solve a 2D case and compared the numerical simulation results with experimental results to verify its VIV estimation procedure. Gamino et al. (2013) developed a new computational method to obtain deep insight of the pipe-soil interaction effects at both free span ends. The simulation revealed a reduction of overall stresses to the free span.

In recent years, researchers began to focus on simulating VIV of free span pipelines by applying linear or nonlinear pipe-soil interaction model. Theti (2001) investigated the steel risers in deep water environments joint industry program and improved the former riser-soil interaction models. The paper also discussed the effects of soil damping and seabed stiffness on riser fatigue life. Bridge et al. (2004) analyzed data set from the STRIDE and CARISIMA JIP to establish a model that can describe the vertical pipe-soil interaction. You (2007) developed a finite difference algorithm which is able to analyze linear or nonlinear soil model. The seafloor support is modeled as plastic springs with constants of soil stiffness.

This thesis presents a fully three dimensional (3D) numerical simulation method of free span pipelines VIV behaviors. The pipeline is modeled as a uniformly distributed tensioned beam. A fully implicit discretization scheme is applied to solve the pipeline motion equations. Flow domain around the pipeline is described by incompressible unsteady Navier-Stokes equations which can be numerically solved.

CHAPTER II

NUMERICAL APPROACH

This Chapter demonstrates the numerical approach for the pipeline VIV simulations, including the pipe motion solver development, computational fluid dynamics method, pipe-soil model and fluid-structure interactions.

Pipeline Motion Solver

A pipeline can be simplified as a tensioned beam in the in-line and cross-flow directions separately. The governing equations of a tensioned beam are as follows:

$$T\frac{d^2y}{dx^2}+\frac{dy}{dx}\frac{dT}{dx}-\frac{d^2}{dx^2}\left(EI\frac{d^2y}{dx^2}\right)+F_y=M\ddot{y}+D_s\dot{y} \tag{1}$$

$$T\frac{d^2z}{dx^2}+\frac{dz}{dx}\frac{dT}{dx}-\frac{d^2}{dx^2}\left(EI\frac{d^2z}{dx^2}\right)+F_z=M\ddot{z}+D_s\dot{z} \tag{2}$$

Here x follows the pipeline axial direction; y denotes the in-line direction and z denotes the cross-flow direction with positive pointing upward. T represents the axial tension; E and I denote Young's modulus and the area moment of inertia respectively. F_y and F_z represent the external forces in their corresponding directions. M denotes the mass of pipeline per unit length and D_s denotes the damping coefficient. A finite difference scheme is used in this study to discretize the governing equation in y direction:

$$\frac{dy}{dx}=\frac{y_{j+1}^{n}-y_{j-1}^{n}}{2\Delta x},\quad j=2,\cdots,N-1 \tag{3}$$

$$\frac{dy}{dx}=\frac{-3y_{j}^{n}+4y_{j+1}^{n}-y_{j+2}^{n}}{2\Delta x},\quad j=1 \tag{4}$$

$$\frac{dy}{dx}=\frac{y_{j-2}^{n}-4y_{j-1}^{n}+3y_{j}^{n}}{2\Delta x},\quad j=N \tag{5}$$

$$\frac{d^2y}{dx^2}=\frac{y_{j-1}^{n}-2y_{j}^{n}+y_{j+1}^{n}}{\Delta x^2},\quad j=2,\cdots,N-1 \tag{6}$$

$$\frac{d^2y}{dx^2}=\frac{y_{j}^{n}-2y_{j+1}^{n}+y_{j+2}^{n}}{\Delta x^2},\quad j=1 \tag{7}$$

$$\frac{d^2y}{dx^2}=\frac{y_{j-2}^{n}-2y_{j-1}^{n}+y_{j}^{n}}{\Delta x^2},\quad j=N \tag{8}$$

$$\frac{d^4y}{dx^4}=\frac{y_{j-2}^{n}-4y_{j-1}^{n}+6y_{j}^{n}-4y_{j+1}^{n}+y_{j+2}^{n}}{\Delta x^4},\quad j=3,\cdots,N-2 \tag{9}$$

$$\frac{d^4y}{dx^4}=\frac{y_{j}^{n}-4y_{j+1}^{n}+6y_{j+2}^{n}-4y_{j+3}^{n}+y_{j+4}^{n}}{\Delta x^4},\quad j=1 \tag{10}$$

$$\frac{d^4y}{dx^4}=\frac{y_{j-1}^{n}-4y_{j}^{n}+6y_{j+1}^{n}-4y_{j+2}^{n}+y_{j+3}^{n}}{\Delta x^4},\quad j=2 \tag{11}$$

$$\frac{d^4y}{dx^4}=\frac{y_{j-3}^{n}-4y_{j-2}^{n}+6y_{j-1}^{n}-4y_{j}^{n}+y_{j+1}^{n}}{\Delta x^4},\quad j=N-1 \tag{12}$$

$$\frac{d^4y}{dx^4}=\frac{y_{j-4}^{n}-4y_{j-3}^{n}+6y_{j-2}^{n}-4y_{j-1}^{n}+y_{j}^{n}}{\Delta x^4},\quad j=N \tag{13}$$

$$\dot{y}=\frac{y_{j}^{n}-y_{j}^{n-1}}{\Delta t},\quad n\geq 2 \tag{14}$$

$$\ddot{y} = \frac{y_j^n - 2y_j^{n-1} + y_j^{n-2}}{\Delta t}, \quad n \geq 3 \tag{15}$$

Here Δx and Δt denote length of a pipeline element and computational time step respectively; n represents current time step. N is the number of segments when discretizing the whole pipeline. Discretization in z direction follows the same scheme as noted. Other parameters except y and z are considered as constants during discretization. The final results in y and z directions are shown separately as follows:

$$\begin{aligned} &\frac{EI}{\Delta x^4} y_{j-2}^n - \left(\frac{T_j}{\Delta x^2} - \frac{1}{2\Delta x}\frac{dT_j}{dx} + \frac{4EI}{\Delta x^4} \right) y_{j-1}^n + \left(\frac{2T_j}{\Delta x^2} + \frac{6EI}{\Delta x^4} + \frac{M}{\Delta t^2} + \frac{D_s}{\Delta t} \right) y_j^n \\ &- \left(\frac{T_j}{\Delta x^2} + \frac{1}{2\Delta x}\frac{dT_j}{dx} + \frac{4EI}{\Delta x^4} \right) y_{j+1}^n + \frac{EI}{\Delta x^4} y_{j+2}^n = F_{y\,j}^n + \left(\frac{2M}{\Delta t^2} + \frac{D_s}{\Delta t} \right) y_j^{n-1} - \frac{M}{\Delta t^2} y_j^{n-2} \end{aligned} \tag{16}$$

$$\begin{aligned} &\frac{EI}{\Delta x^4} z_{j-2}^n - \left(\frac{T_j}{\Delta x^2} - \frac{1}{2\Delta x}\frac{dT_j}{dx} + \frac{4EI}{\Delta x^4} \right) z_{j-1}^n + \left(\frac{2T_j}{\Delta x^2} + \frac{6EI}{\Delta x^4} + \frac{M}{\Delta t^2} + \frac{D_s}{\Delta t} \right) z_j^n \\ &- \left(\frac{T_j}{\Delta x^2} + \frac{1}{2\Delta x}\frac{dT_j}{dx} + \frac{4EI}{\Delta x^4} \right) z_{j+1}^n + \frac{EI}{\Delta x^4} z_{j+2}^n = F_{z\,j}^n + \left(\frac{2M}{\Delta t^2} + \frac{D_s}{\Delta t} \right) z_j^{n-1} - \frac{M}{\Delta t^2} z_j^{n-2} \end{aligned} \tag{17}$$

In this research, pipeline parameters E, I, T, M, D_s and N are given before conducting the computation. External forces F_y and F_z are obtained from the fluid solver which is described in the last section of this Chapter. The only unknowns are displacements of the pipeline at each computational node.

Equation (16) and (17) can be solved in matrix forms:

$$[K][X] = [F] \tag{18}$$

Here K is a matrix of dimension $N \times N$. It is extracted from the left sides of equation (16) and (17) and denotes the stiffness of the tensioned beam. Matrix

$X = \begin{pmatrix} y_1 \\ y_2 \\ \vdots \\ y_N \end{pmatrix}$ or $\begin{pmatrix} z_1 \\ z_2 \\ \vdots \\ z_N \end{pmatrix}$ denotes the pipeline displacements at each computational node.

Matrix F includes the inertia, damping and external force terms from the right sides of equation (16) and (17). The accuracy of this pipeline motion solver is verified by Xiao (2015).

Computational Fluid Dynamics Background

The flow domain around the pipeline can be computed by numerically solving the Reynolds Averaged Navier-Stokes (RANS) equations. The RANS equations are solved in time domain by running the Finite Analytic Navier-Stokes (FANS) code which is utilized and validated in many published papers from Chen et al. (1988, 1989, 1990 and 2013). The turbulence model in the code is a large eddy simulation (LES) model.

Overset grid, also called Chimera grid (Meakin et al., 1999), is used in this study for dynamically simulating pipeline motion in a uniform current. The most common difficulty that researchers would note in the CFD simulation is that most geometries cannot be well described by using a simple and contiguous grid. In many cases, different type of grids are needed to represent different geometrical characteristics. An appropriate method is to divide the fluid field into several subdomains and mesh each one with specific grid scheme. These subdomains are also referred as blocks, which have overlapping areas at the interface between every two adjacent blocks. Boundary information is communicated between these blocks via interpolation at the fringe points. Some grid points are called hole points because they are not used in the solution (Peterson, 1999). In general, three steps are necessary for applying the overset grid method:

1. Grid generation
2. Hole cutting
3. Interpolation

A typical overset grid is shown in Figure 1. The red grid around the surface of the pipe is in polar coordinate while the green grid is in Cartesian coordinate. The right-handed coordinate system is set up as: x denotes pipe axial direction, y follows the current direction, and z direction coincides with the cross flow direction. Generally, structured-curvilinear grid combined with Cartesian grid are often applied in complex geometries. When several geometric components occur in one fluid domain, their specific body fitting curvilinear grid can be generated independently, and then embedded into the same Cartesian background grid.

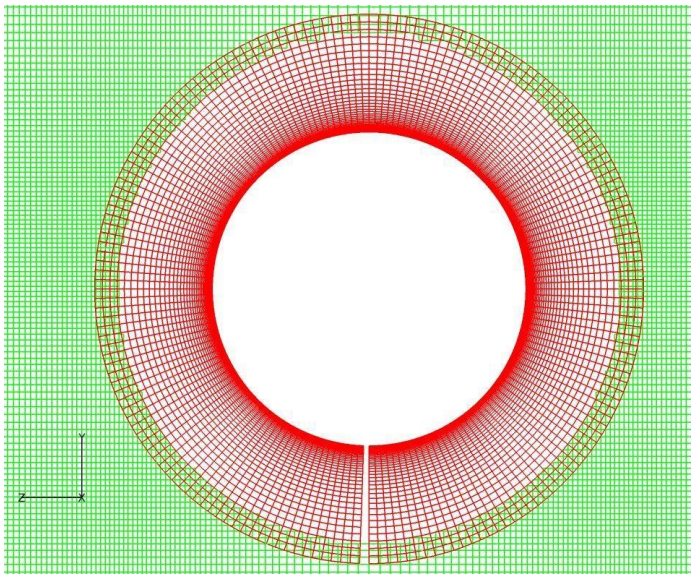

Figure 1 Typical Overset Grid

In this thesis, PEGSUS 4.0 (Suhs et al., 1991) is used to conduct the hole cutting part of the grid generation. It is a fully 3D code. PEGSUS 4.0 adds further flexibility to the user inputs and control of the overall process. The exclusion process of points is finished by defining a hole domain in the red grid within which the green grid points will be blanked. The points in the green grid surrounding the blanked points form a hole

boundary which will receive the flow field information interpolated from red grid points. On the other hand, points on the outer boundary of the red block will also receive the flow field information interpolated from green grid points.

Applying overset grid method allows us to manipulate the resolution of one particular part of the grid without changing the other portions. To be more specific in this thesis, the computational grid is modified to very fine resolution near the pipeline outer boundary and the sea bottom boundary, whereas the far field grid is relatively coarse. This strategy reduces the total grid element number and leads to a great economization of calculation time.

To deal with a pipeline VIV problem, it is necessary for us to use at least three grid blocks to numerically simulate the whole fluid field: near body grid, wake grid and background grid. A typical cross section view of this strategy is shown in Figure 2. The near body grid (red) is generated in the polar coordinate. The white color circular area covered by red grid is the cross section of the pipeline, which is treated as a solid boundary during the CFD modeling process. The wake grid (green) is generated in the Cartesian coordinate surrounding the near body grid. In this wake area, the grid is fine enough for vortex shedding and propagation. In the overlapping area between near body grid and wake grid, the sizes of both grids from each block are of nearly same value to guarantee the accuracy of exchanging the flow domain information. The background grid (blue) is also generated in the Cartesian coordinate. The background grid is relatively coarse compared to the other two grid blocks due to a demand of reducing the total number of grid points without hurting accuracy. There is a rectangular hole cut by

the wake grid within the background grid as it follows the same cutting and interpolation process mentioned before. The grid magnitude at the inner boundary of the background grid is approximately the same as that at the outer boundary of the wake grid. This again ensures a smooth information transition between two adjacent computational blocks.

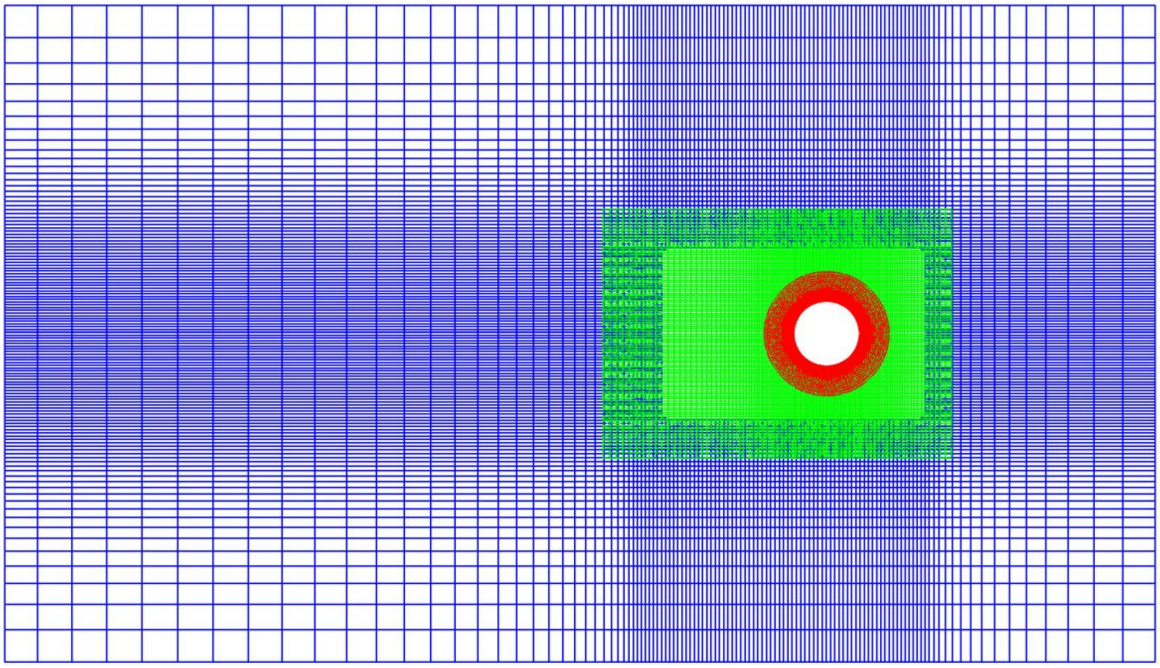

Figure 2 2D Cross Section Grid for VIV Simulation

The 2D meshing approach mentioned above can only discretize the flow domain at each cross section. We also need to divide the flow domain into many parallel layers along the pipeline axial direction to complete the whole 3D meshing process. As noted before, the current in this study is propagating perpendicular to the axial direction in the in-line direction and remains a constant velocity value along the axial direction. Therefore, it is feasible to divide the axial direction into relatively coarse grid.

A moving grid scheme is also applied in this study. As the pipeline moves, the near body grid and the wake grid will move at the same velocity. Meanwhile, the background grid will remain stationary during the calculation. It is guaranteed that there is no gap between the pipeline boundary and the fluid boundary by applying this synchronous moving approach. Finally, the most important advantage of this grid generation strategy is that there is no need to regenerate grid at each time step and hence a huge reduction of calculation time.

Soil Models

When considering the deep water pipe-soil interaction, a linear soil model can be found in the DNV-RP-F105 (2006) recommended practice for modeling free span pipelines. Soil effect is significant both in the dynamic response of the free span pipeline. In the linear soil model, the soil is simplified as horizontal and vertical springs with equivalent damping and stiffness. Figure 3 shows the spring-pipeline system.

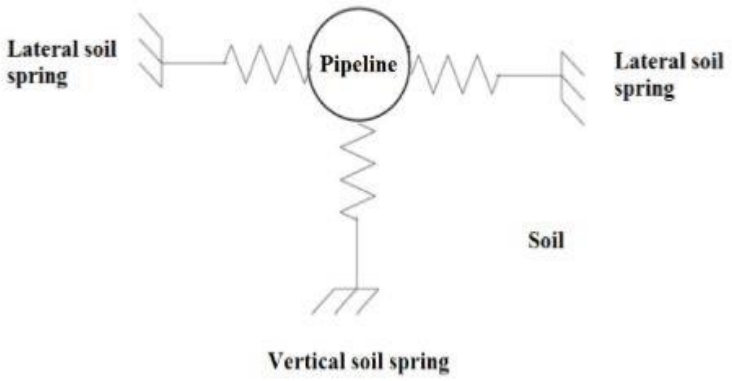

Figure 3 Sketch of Spring-Pipeline System

To determine the horizontal and vertical dynamic stiffnesses, the following empirical formulas are given by the DNV-RP-F105:

$$K_L = C_L \cdot (1+\upsilon) \cdot \left(\frac{2}{3} \frac{\rho_s}{\rho} + \frac{1}{3} \right) \cdot \sqrt{D} \tag{19}$$

$$K_V = \frac{C_V}{1-\upsilon} \cdot \left(\frac{2}{3} \frac{\rho_s}{\rho} + \frac{1}{3} \right) \cdot \sqrt{D} \tag{20}$$

Here K_L and K_V denote the horizontal and vertical dynamic stiffness respectively. C_L and C_V denote the corresponding dynamic stiffness factors. υ represents Poisson's

ratio and ρ_s/ρ is density ratio of the pipeline over water. D denotes the outer diameter of the pipeline. The dynamic stiffness factors are given in Table 1 and Table 2 for pipe-soil interactions in sand and clay from the recommended practice.

Table 1 Dynamic Stiffness Factors for Sand Type Soil

Sand Type	C_L (kN/m$^{5/2}$)	C_V (kN/m$^{5/2}$)
Loose	9000	10500
Medium	12500	14500
Dense	18000	21000

Table 2 Dynamic Stiffness Factors for Clay Type Soil

Clay Type	C_L (kN/m$^{5/2}$)	C_V (kN/m$^{5/2}$)
Very Soft	500	600
Soft	1200	1400
Firm	2600	3000
Stiff	3900	4500
Very Stiff	9500	11000
Hard	10500	12000

Soil damping also need to be considered in the pipe-soil interaction model. Both soil type and the length of the pipeline (quantized in the form of *L/D*) can affect the damping ratio. The damping ratios are given in Table 3 and Table 4 for pipe-soil interactions in sand and clay from the recommended practice.

Table 3 Soil Damping Ratios for Sand Type Soil

Sand Type	*L/D* (in-line direction)			*L/D* (cross-flow direction)		
	<40	100	>160	<40	100	>160
Loose	3.0	2.0	1.0	2.0	1.4	0.8
Medium	1.5	1.5	1.5	1.2	1.0	0.8
Dense	1.5	1.5	1.5	1.2	1.0	0.8

Table 4 Soil Damping Ratios for Clay Type Soil

Sand Type	*L/D* (in-line direction)			*L/D* (cross-flow direction)		
	<40	100	>160	<40	100	>160
Loose	3.0	2.0	1.0	2.0	1.4	0.8
Medium	1.5	1.5	1.5	1.2	1.0	0.8
Dense	1.5	1.5	1.5	1.2	1.0	0.8

To obtain a more complex and accurate simulation of pipe-soil interaction, Aubeny and Biscontin (2006) presented a nonlinear soil model. They also considered the pipeline-soil interaction problem as a spring-pipeline system while the stiffness characteristics are expressed by using a nonlinear force-displacement (*P*-*z*) curves. The system can be described by the following nonlinear governing equation:

$$EI\frac{d^4z}{dx^4} = W - P \tag{21}$$

Here *EI* is the bending stiffness of the pipeline and *W* denotes the pipeline weight per unit length. The force term *P* refers to the soil resistance force per unit length and *z* represents displacement of the pipeline in the cross-flow direction.

The general load-deflection behavior pattern is produced by Dunlap et al. (1990) based on model tests. As shown in Figure 4, Path 0-1, which is named as Backbone Curve, refers to the first penetration of the pipeline into the sea bottom soil. When the pipeline goes uplift, the *P*-*z* curve will carry on by following Path 1-2. Model tests reveal that the pipeline will separate from the soil at sufficiently large uplift motion magnitude and the *P*-*z* curve follows Path 2-3 which gradually tends toward zero. The pipeline is completely detached from the sea bottom soil during the continued uplift. Then, deflection reverses, the pipeline moves downward again and retouches the soil at Point 3 in the *P*-*z* curve. Data from the model tests also show that the soil resistance grows up gradually as depicted by Path 3-1 in Figure 4 rather than mobilizing abruptly upon retouch. Further deflections can either repeat uplift along Path 1-2 or deepen the trench along Path 1-1’ depending on the pipeline motion time history. What is noteworthy is

that deflection reversals can appear from any intermediate points along the paths as marked by dashed lines in Figure 4.

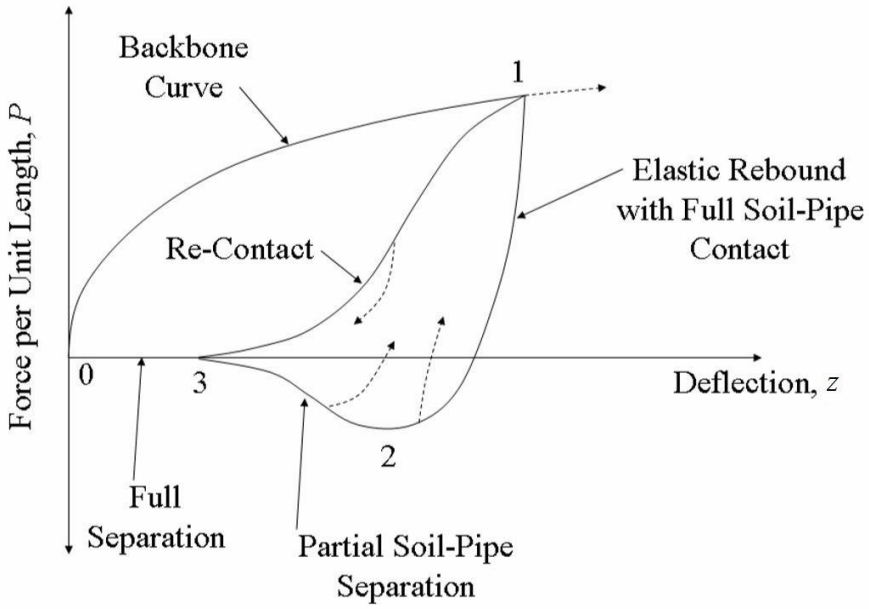

Figure 4 Typical *P*-*z* Behavior Pattern

For the Backbone Curve, the soil resistance force *P* can be described by the following formulas where *c* refers to the soil strength and N_p is a dimensionless bearing factor:

$$P = N_p \cdot cD \tag{22}$$

$$N_p = a \cdot \left(z / D \right)^b \tag{23}$$

For the Unload-Reload Loop, we need to employ a mathematical formulation. As discussed above, Figure 4 contains the loop which can be described in terms of three fixed points: Point 1 (P_1, z_1) initiates the unload-reload cycle; Point 2 (P_2, z_2) is the point

at the maximum tension; Point 3 (P_3, z_3) is the detaching point. These points are related by two parameters which can be measured in model tests:

$$P_2 = -\phi \cdot P_1 \tag{24}$$

$$\left(z_2 - z_3\right) = \psi \cdot \left(z_1 - z_2\right) \tag{25}$$

A hyperbolic relationship defines the *P*-*z* curve between Point 1 and 2:

$$P = P_1 + \frac{z - z_1}{\frac{1}{k_o} + \chi \frac{z - z_1}{\left(1+\omega\right) P_1}} \tag{26}$$

Here, parameters k_o and ω can be estimated from model tests as well. The parameter χ is simply a sign mark which equals to -1 for unloading and 1 for loading.

A cubic relationship defines the *P*-*z* curve between Point 2 and 3:

$$\begin{aligned} P &= \frac{P_2}{2} + \frac{P_2}{4}\left[3\left(\frac{z - z_0}{z_m}\right) - \left(\frac{z - z_0}{z_m}\right)^3\right] \\ y_0 &= \frac{z_2 + z_3}{2} \\ y_m &= \frac{z_2 - z_3}{2} \end{aligned} \tag{27}$$

A similar cubic relationship defines the *P*-*z* curve between Point 3 and 1:

$$\begin{aligned} P &= \frac{P_1}{2} + \frac{P_1}{4}\left[3\left(\frac{z - z_0}{z_m}\right) - \left(\frac{z - z_0}{z_m}\right)^3\right] \\ y_0 &= \frac{z_1 + z_3}{2} \\ y_m &= \frac{z_1 - z_3}{2} \end{aligned} \tag{28}$$

Finally, all the parameters mentioned above are listed in the following table:

Table 5 *P-z* Model Parameters

Parameter	Value
a	6.70
b	0.254
k_o/c	660
ω	0.433
ϕ	0.203
ψ	0.661

Murff et al. (1989) also presented a nonlinear soil model which has a different expression for the bearing factor:

$$N_p = (4 + 2\pi) \cdot \sqrt{(z/D) + (z/D)^2} \tag{29}$$

This thesis applies the two nonlinear soil models introduced above to model the pipe-soil interactions in order to conduct more accurate and realistic numerical simulations of free span pipeline VIV behaviors. The results are compared with those using a linear soil model and validated by the recommended practice DNV-RP-F105 (2006).

Fluid-Structure Interactions

Analytically solving fluid-structure interaction (FSI) problems is usually quite difficult so that we need to utilize experiments or numerical simulation methods. Monolithic approach and Partitioned approach are two main approaches for solving these problems. In this study, we rely on a Partitioned approach: the governing equations of the flow and the pipeline motion are solved separately with two distinct solvers (Bungartz et al., 2006). The basic FSI solving procedure is shown in Figure 5. The pipeline motion solver mentioned before is called as a subroutine by the fluid solver. The Navier-Stokes equation is numerically solved and the velocity and pressure of the whole flow field is obtained by this system at each time step. The lift and drag forces are calculated along the pipeline and read by the pipeline motion solver mentioned before as input. At the same time, the motion solver returns the information of the pipeline velocity and displacement back to the fluid solver for next time step computation.

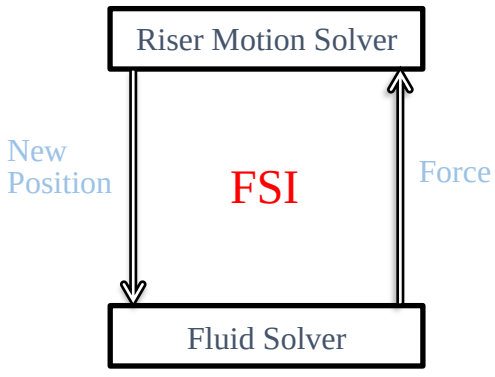

Figure 5 Fluid-Structure Interaction Procedure

During the process of solving the fluid field, we need to specify the boundary conditions and the initial conditions. The pipeline surface is considered as the inner boundary of the fluid field and the pipeline position and velocity is treated as moving boundary.

During the process of solving the pipeline motion, we need to calculate external forces. Based on the CFD calculation results above, normal and shear forces are obtained by integrating the given velocity and pressure information along the surface of the pipeline. As noted before, relatively coarse grid is applied in the fluid field due to its insignificant change along the axial direction. In this research, 30 segments (31 layers) are enough for smoothly describing the axial flow field change. On the other hand, we use 240 (30×8) segments to divide the pipeline and simulate its profile and displacement more accurately. It is worthy to note that there is a 1:8 mapping relation between the fluid solver and the pipeline motion solver. The force mapping relationship is shown in Figure 6.

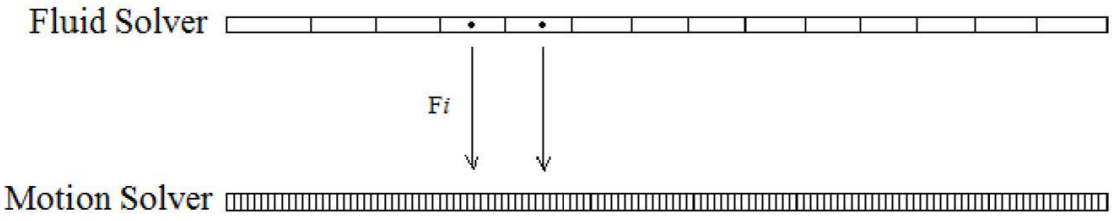

Figure 6 Force Mapping Relationship

CHAPTER III

COMPARISON BETWEEN SOIL MODELS

As mentioned above, Xiao (2015) conducted a numerical simulation of a free span pipeline using the linear pipe-soil interaction model provided by DNV-RP-F105 (2006). In his thesis, a free span pipeline depicted in Figure 7 was analyzed. The length to diameter ratio of the pipeline is L/D=300. Two ends (point A and point D) are fixed and two sides (segment AB and segment CD) are partially embedded in the soil. The middle segment BC is suspended with a free span length L_s/D=150. The gap to diameter ratio is chosen as G/D=2.0. More parameters about the pipeline are listed in Table 6.

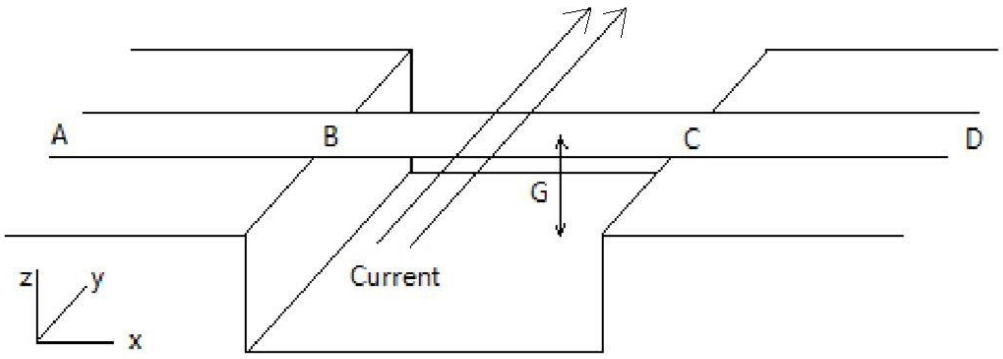

Figure 7 Free Span Pipeline Lying on the Soil Seabed

In Xiao's thesis, the soil model is included at the bottom boundary below the gap as well. This allows the pipeline to dig into bottom soil and interact with the soil model when the VIV amplitude exceeds the gap depth. Otherwise, the pipeline motion will change suddenly and may cause unphysical results.

Table 6 Parameters of a Free Span Pipeline

Parameter	Value
Total Length L	3.8 m
Outer Diameter D	12.7 mm
Bending Stiffness EI	130.0 Nm^2
Weight Per Unit Length W	3.038 N/m
Pretention T	500 N

To validate the nonlinear pipe-soil interaction model, a numerical simulation of the same free span pipeline is conducted in this research and the results will be compared.

Grid Generation

Grid generation is the first important thing for numerical simulation. An overset grid scheme is applied in this research as noted before. In this case, we use 6 blocks to cover the whole fluid domain. Figure 8 and Figure 9 show the near view of middle section and side section of the fluid field respectively. The near body block (red) consists of 231322 (31×182×41) grid points; the wake block (green) consists of 178281 (31×81×71) grid points; the background block (blue) consists of 255316 (31×116×71) grid points; the top near wall block (black) consists of 75516 (31×116×21) grid points; the gap block (yellow) consists of 38976 (16×116×21) grid points; the bottom near wall grid (black) consists of 27840 (16×116×15) grid points. Thus, there are 807251 (about 0.8 million) computational nodes in total.

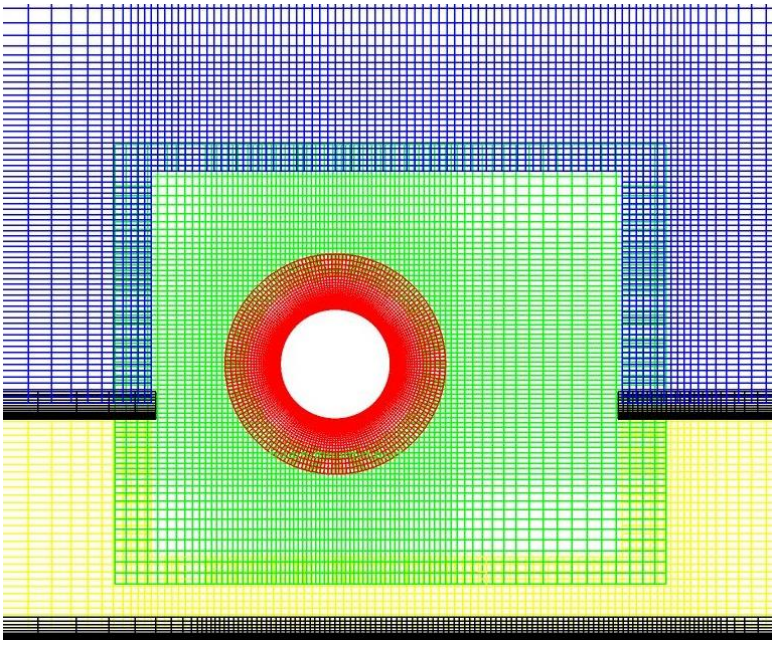

Figure 8 Near View of the Middle Section

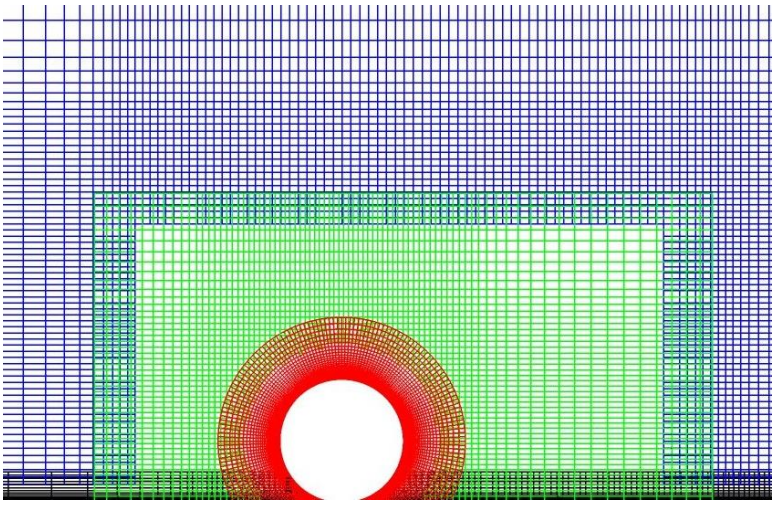

Figure 9 Near View of the Side Section

The pipeline is placed in the middle of the cross-flow direction in the flow field. The flow inlet boundary is 10*D* in front of the pipeline center while the flow outlet boundary is 30*D* behind the pipeline center. The cross-flow direction ranges from -10*D* to 10*D*. The uniform current propagates along the in-line direction.

It is noteworthy that the red block represents the flow field around the pipeline, not the pipeline cross section. Thus, the inner boundary of the red block is the outer boundary of the pipeline cross section. The red block consists of 31×182×41 grid points with 30 elements in the axial direction, 180 elements in the circumferential direction and 40 elements in the radial direction. What is worthy to note is that in the circumferential direction, only 180 elements are created by 182 grid points as node #181 overlaps node #1 and node #182 overlaps node #2. This overlapping allows the near body grid boundaries which are represented by black lines in Figure 10 to obtain the flow information.

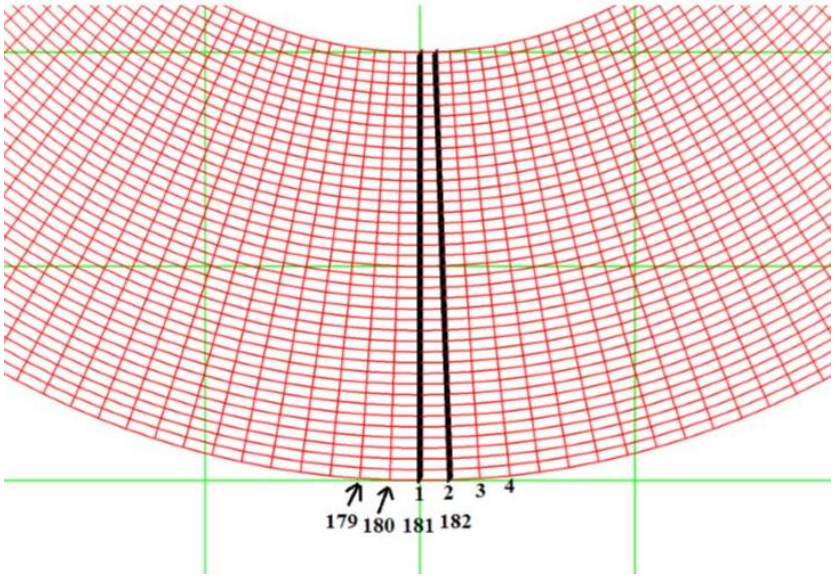

Figure 10 Circumferential Grid

As mentioned above, the flow field changes more dramatically as it reaches closer to the pipeline center such that it requires finer grid in the pipeline surrounding area. This allows us to capture small changes, especially vortex shedding in that area. Therefore, grid refinement needs to be carried out. For all the grid blocks, the closer to the pipeline center, the finer grid we have after refinement. Take the near body and wake blocks as an example, Figure 11 depicts a near view of the refinement result. To be more specific in this example, we need to set the size of the near body grid at the outer boundary as approximately the same size of the nearby wake grid. This strategy guarantees no distortion during the interpolation process between two blocks.

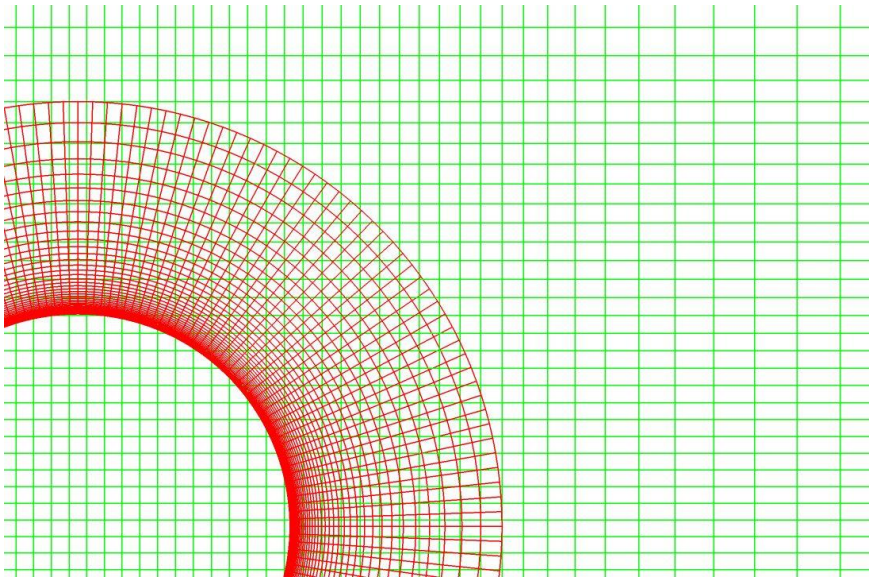

Figure 11 Near View of the Refinement Result

The next step is hole cutting where there is no need to illustrate the process again as we have discussed it in last Chapter. Figure 12 depicts the result of the wake grid after hole cutting.

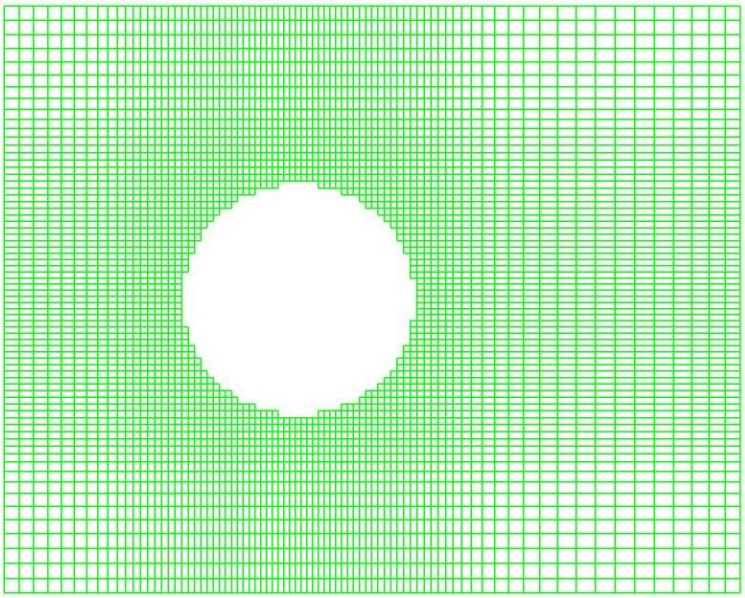

Figure 12 Hole Cutting Result of Wake Grid

Finally, we need to apply a different scheme to generate different computational grid for the pipeline segments which are embedded in the soil. The flow field will be cut by the boundary layer between water and soil. A dynamic grid scheme is applied. The grid around the pipeline, the red block and the green block, will be regenerated at every time step as the pipeline vibrates up and down. Other blocks will be fixed at their original positions during the simulation process.

Simulation Results

As the uniform sea bottom currents pass by the gap, the pipeline presents the in-line deflection and cross-flow vibration which is recorded in Figure 13 and 14. To illustrate the effects of soil, large stiffness referred to soil type of dense sand is applied in this case. When the pipeline moves downward, two side parts are stopped due to the soil resistance force. When the pipeline moves upward, the whole pipeline will leave the sea bottom. What is noteworthy is that the in-line motion shows no restricted zones because the whole pipeline is above the soil during its deflection in the in-line direction.

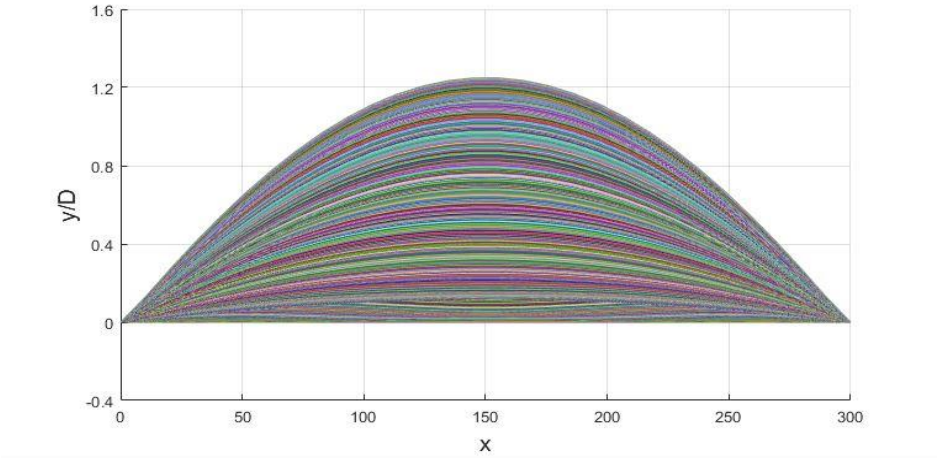

Figure 13 In-Line Envelope

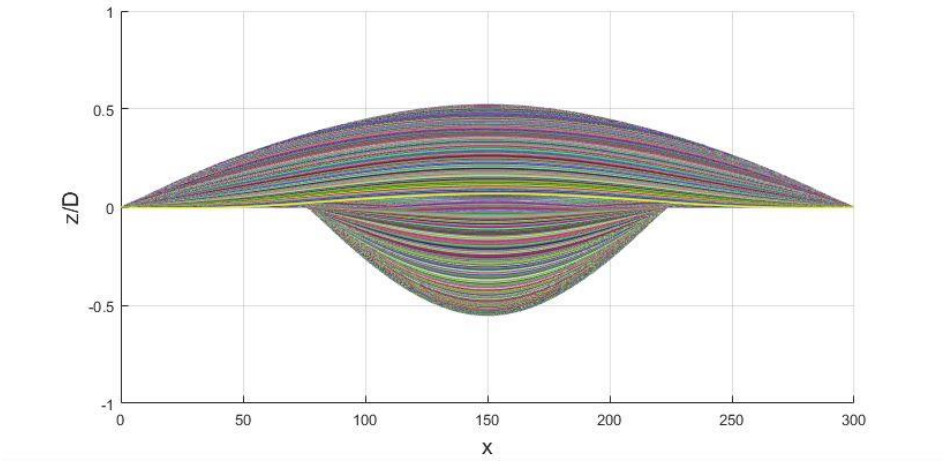

Figure 14 Cross-Flow Envelope

The pipeline deflection and vortex shedding is visualized in Figure 15. The deflection is relatively small compared to the general scale. The vorticity field is shown in the axial direction by setting up several parallel planes. It can be observed from the figure that the vortices are in a 2S pattern and travel downstream. The near bottom vortices dissipate quickly and mix into the uniform current in the wake flow.

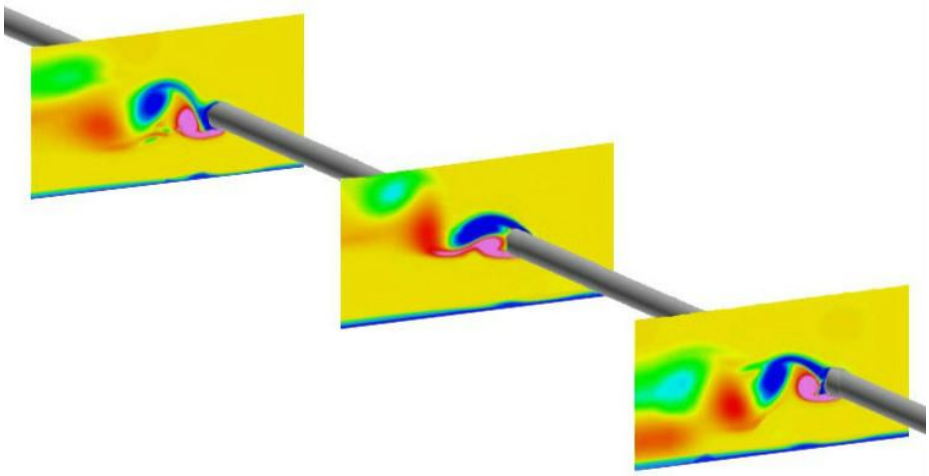

Figure 15 Pipeline Deflection and Vorticity Contours

A linear and two nonlinear soil models are compared in this thesis. The expressions below are derived from linear soil model, Aubeny's nonlinear soil model and Murff's nonlinear soil model respectively. The dimensionless bearing factor N_p is a function of penetration depth for all the three soil models. The soil resistance force can be obtained from the bearing factor as the force is proportional to it. Parameters in the expressions are chosen as recommended values as noted before.

$$N_p = \frac{K_V}{c} \cdot \left(z / D \right) \tag{30}$$

$$N_p = a \cdot \left(z / D \right)^b \tag{31}$$

$$N_p = \left(4 + 2\pi \right) \cdot \sqrt{\left(z / D \right) + \left(z / D \right)^2} \tag{32}$$

Figure 16 shows the theoretical estimated load-deflection relationships of the three soil models. When the penetration depth is relatively small (approximately less than 0.1), the bearing factor of linear soil model is smaller than the nonlinear soil models which indicates linear soil model behaves 'softer' during the compression. When the penetration grows larger, nonlinear soil models will produce much smaller resistance forces.

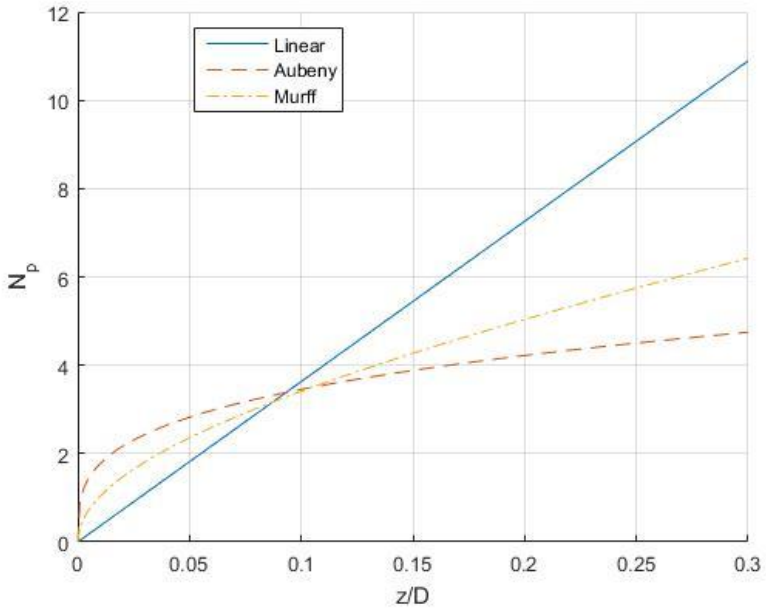

Figure 16 Load-Deflection Relationships of Three Soil Models

Numerical simulation results are also needed to compare the three soil models. A medium sand type soil is picked to compare the VIV simulation results of small penetration while a soft clay type soil is selected for computation of large penetration. Two points of the pipeline are analyzed: Point N at the edge of soil in Figure 17 is named as ‘soil point’ and Point M, the middle point of the whole pipeline, where the maximum deflection occurs is named as ‘span point’. In this case, the uniform current speed is set to be 0.2m/s.

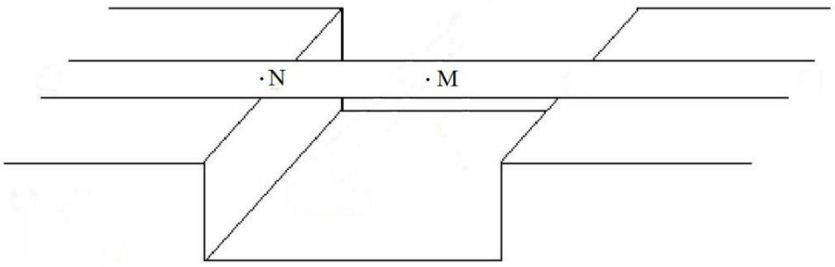

Figure 17 Definition of Selected Points

For the medium sand type soil, Figure 18 to 20 shows the pipeline motion history of selected points in cross-flow directions using linear soil model, soil model of Aubeny et al. (2006) and soil model of Murff et al. (1989) respectively. Figure 18 (a), 19 (a) and 20 (a) record the cross-flow motion history of the soil point. When the pipeline moves downward, the soil resistance force will restrict the pipeline penetration depth. We can see exactly the difference between these soil models: the vibration amplitudes at soil point using linear soil model are around 0.08 which is larger than those using nonlinear soil models because the maximum penetration depth is relatively small (less than 0.1). This is a typical result with sand type soil due to the large soil stiffness. Result of soil model of Aubeny et al. (2006) is also slightly different from soil model of Murff et al. (1989) as it behaves 'firmer'. Figure 18 (b), 19 (b) and 20 (b) record the cross-flow motion history of the span point. Results of nonlinear soil models are approximately the same. What is noteworthy is that for the linear soil model result, vibration amplitudes below z/D=0 are around 0.8 which is smaller than the amplitudes above z/D=0. No obvious difference of the vibration frequency can be observed from these results.

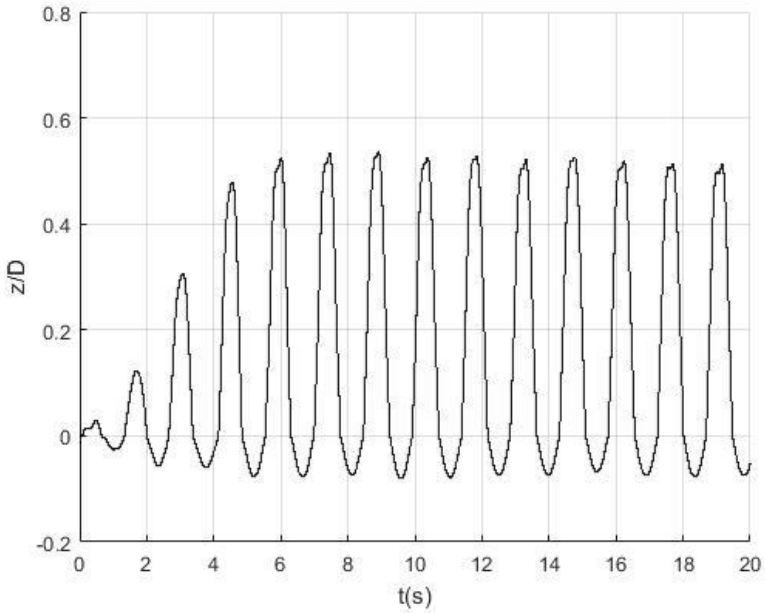

(a)

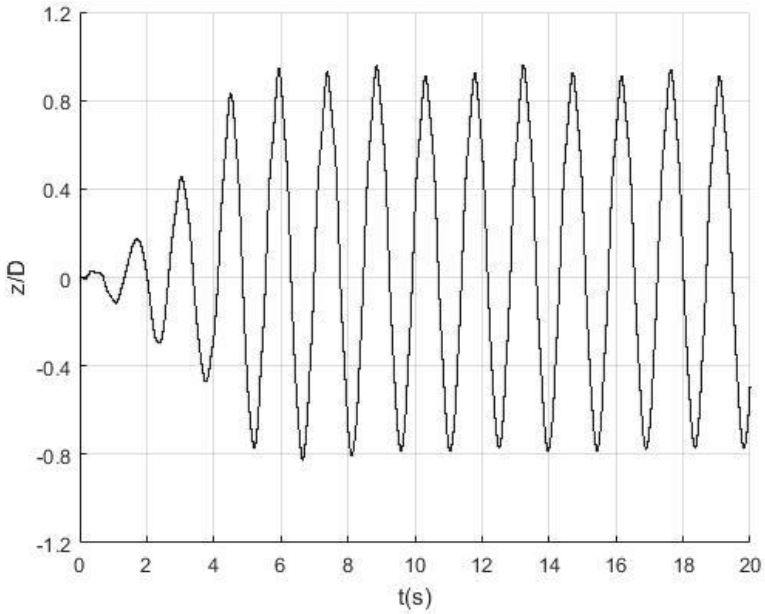

(b)

Figure 18 Pipeline Cross-Flow Motion History Using Linear Soil Model with Sand Type Soil (a) Soil Point (b) Span Point

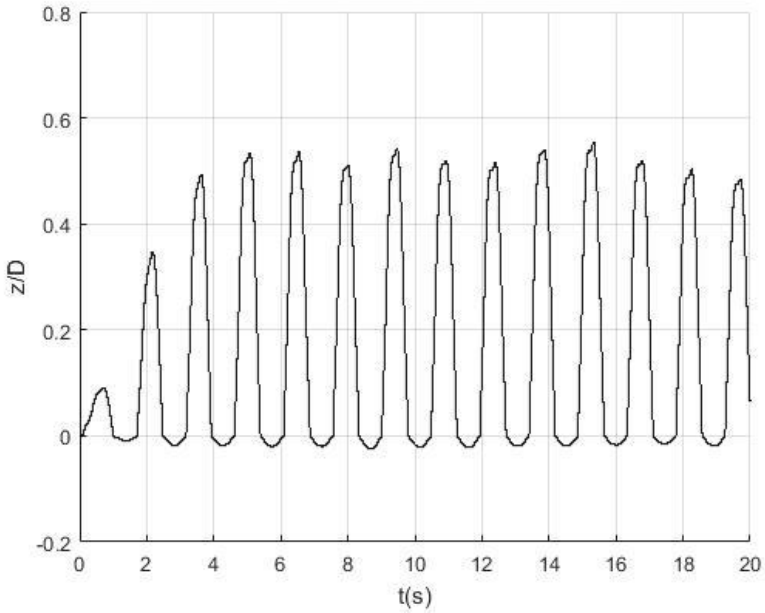

(a)

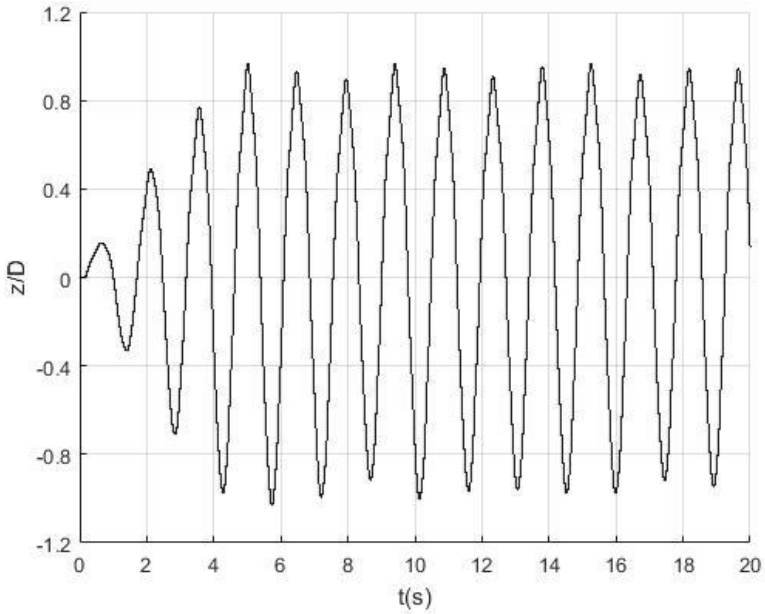

(b)

Figure 19 Pipeline Cross-Flow Motion History Using Soil Model of Aubeny et al. (2006) with Sand Type Soil (a) Soil Point (b) Span Point

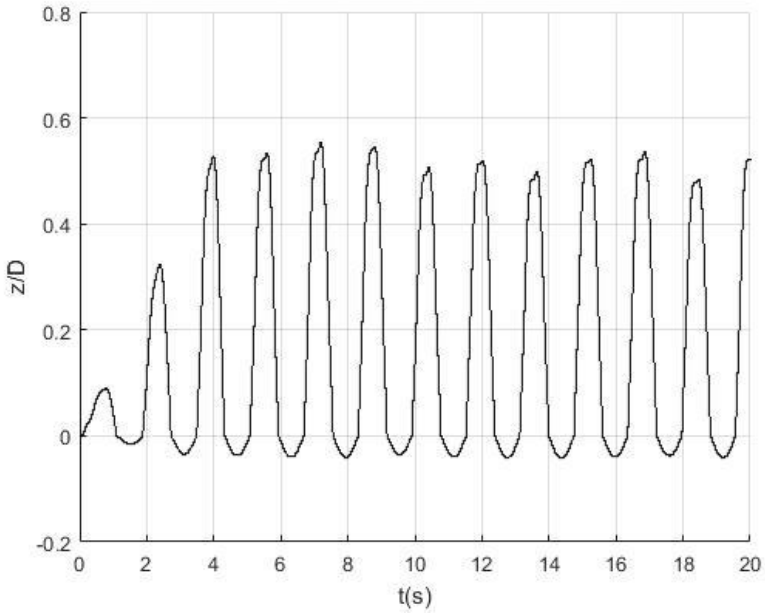

(a)

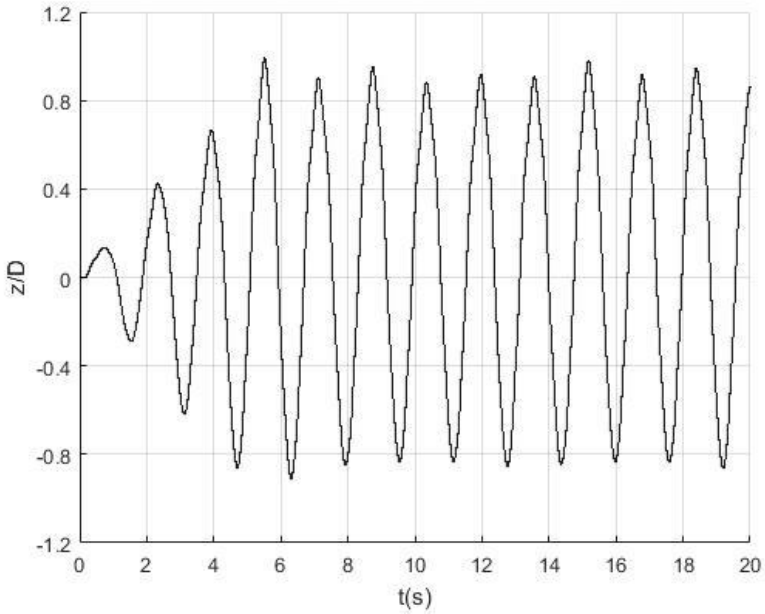

(b)

Figure 20 Pipeline Cross-Flow Motion History Using Soil Model of Murff et al. (1989) with Sand Type Soil (a) Soil Point (b) Span Point

To obtain deep insight of the effects of soil type, we also analyzed a case with soft clay type soil. Figure 21 to 23 shows the pipeline motion history of selected points in cross-flow directions using linear soil model, soil model of Aubeny et al. (2006) and soil model of Murff et al. (1989) respectively. The cross-flow motion history of the soil point is recorded in Figure 21 (a), 22 (a) and 23 (a). It can be observed that the penetration depth is much larger than the results of sand type soil. Vibration amplitude of the penetration at soil point using nonlinear soil models is about 0.2 and obviously larger than the amplitude using linear soil model. The main reason for this reversal is due to the relatively large maximum penetration into the seabed soil. As shown in Figure 21 (b), 22 (b) and 23 (b), the vibration amplitude of the span point using soil model of Aubeny et al. (2006) is the largest among the three soil models. It is observed from the simulation results that the vibration amplitudes at the span point using linear soil model are approximately 10% smaller than those using nonlinear soil models. Again, for the linear soil model result, vibration amplitudes below z/D=0 are around 0.8 which is smaller than the amplitudes above z/D=0. In addition, vibration frequencies are independent of the soil type.

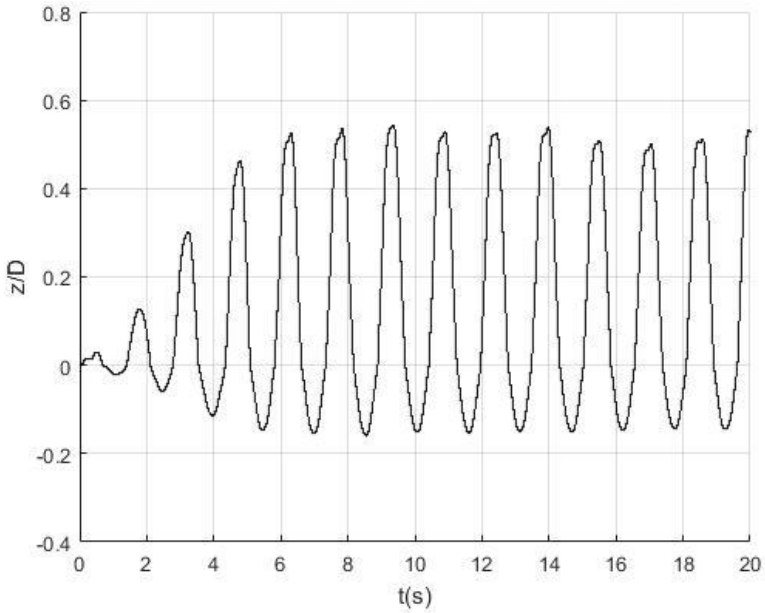

(a)

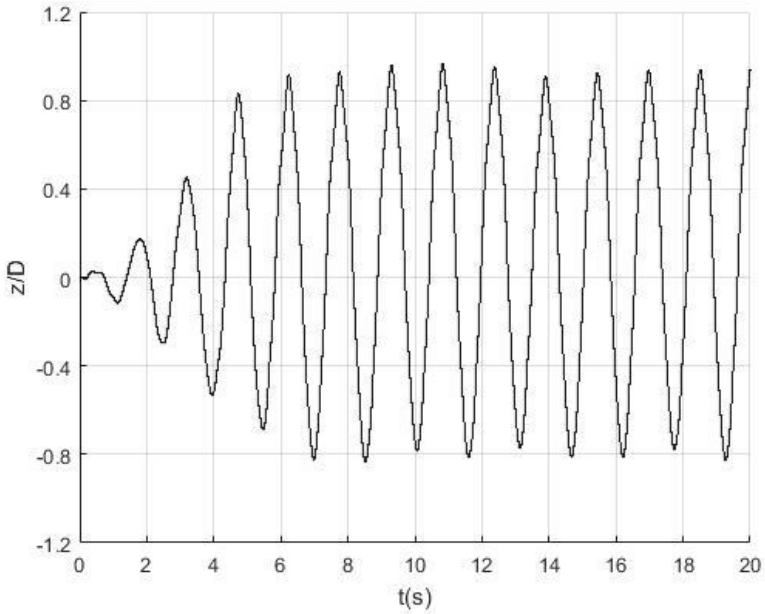

(b)

Figure 21 Pipeline Cross-Flow Motion History Using Linear Soil Model with Clay Type Soil (a) Soil Point (b) Span Point

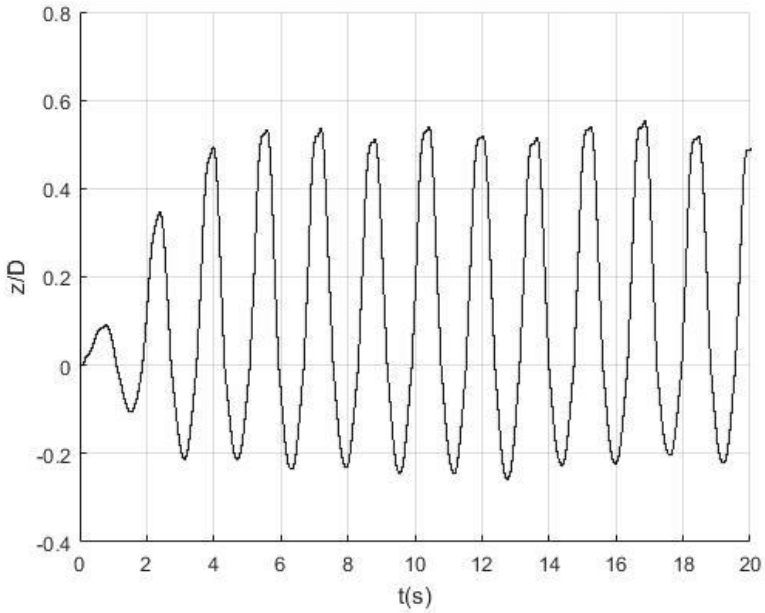

(a)

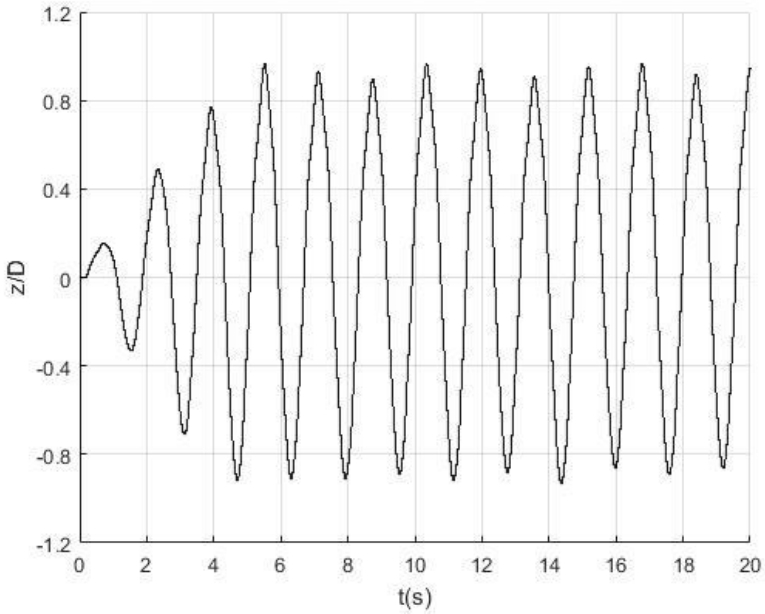

(b)

Figure 22 Pipeline Cross-Flow Motion History Using Soil Model of Aubeny et al. (2006) with Clay Type Soil (a) Soil Point (b) Span Point

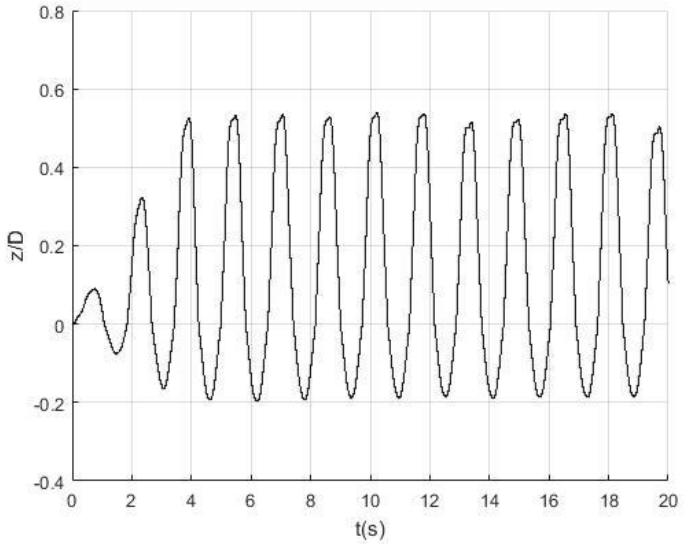

(a)

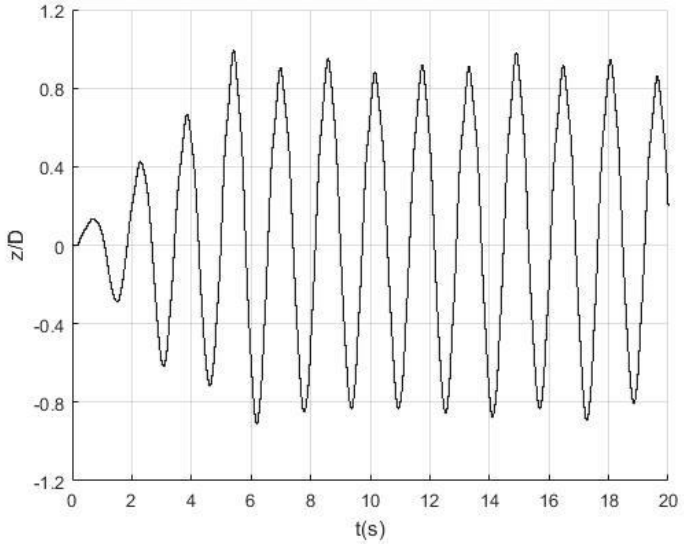

(b)

Figure 23 Pipeline Cross-Flow Motion History Using Soil Model of Murff et al. (1989) with Clay Type Soil (a) Soil Point (b) Span Point

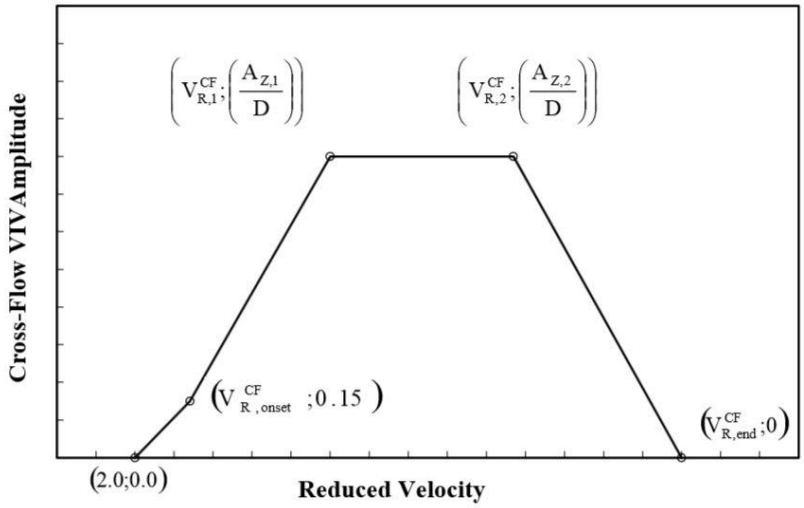

Figure 24 Free Span Pipeline Response Model from DNV (2006)

For the response of a free span pipeline, DNV-RP-F105 (2006) recommended two models: the Force model and the Response model. The Force model is used for modeling free span response under hydrodynamic loads while the Response model is suitable for modeling response dominated by VIV. In this thesis, waves are neglected and only the effect of uniform sea bottom currents is considered. Therefore, we use the Response model to validate our simulation results. The Response model for the cross-flow amplitude response is illustrated by Figure 24 and the following formulas:

$$V_{R,onset}^{CF} = \frac{3 \cdot \Psi_{proxi,onset} \cdot \Psi_{trench,onset}}{\gamma_{on,CF}} \tag{33}$$

$$V_{R,1}^{CF} = 7 - \frac{\left(7 - V_{R,onset}^{CF}\right)}{1.15} \cdot \left(1.3 - \frac{A_{Z,1}}{D}\right) \tag{34}$$

$$V_{R,2}^{CF} = V_{R,end}^{CF} - \left(\frac{7}{1.3}\right) \cdot \left(\frac{A_{Z,1}}{D}\right) \tag{35}$$

$$V_{R,end}^{CF} = 16 \tag{36}$$

$$\left(\frac{A_{Z,1}}{D}\right) = \begin{cases} 0.9 & \alpha > 0.8 \quad \frac{f_{n+1,CF}}{f_{n,CF}} < 1.5 \\ 0.9 + 0.5 \cdot \left(\frac{f_{n+1,CF}}{f_{n,CF}} - 1.5\right) & \alpha > 0.8 \quad 1.5 \le \frac{f_{n+1,CF}}{f_{n,CF}} \le 2.3 \\ 1.3 & \alpha > 0.8 \quad \frac{f_{n+1,CF}}{f_{n,CF}} > 2.3 \\ 0.9 & \alpha \le 0.8 \quad KC > 30 \\ 0.7 + 0.01 \cdot (KC - 10) & \alpha \le 0.8 \quad 10 \le KC \le 30 \\ 0.7 & \alpha \le 0.8 \quad KC < 10 \end{cases} \tag{37}$$

$$\left(\frac{A_{Z,2}}{D}\right) = \left(\frac{A_{Z,1}}{D}\right) \tag{38}$$

Here $V_R = \frac{U_c + U_w}{f_n D} = \frac{U_c}{f_n D}$ means the reduced velocity which ranges from 2 to 16 in this case. Another parameter $\alpha = \frac{U_c}{U_c + U_w} = 1$ denotes the current flow velocity ratio. $\frac{f_{n+1,CF}}{f_{n,CF}}$ is the cross-flow frequency ratio which is measured as 2.0 in our test. The Keulegan-Carpenter number $KC = \frac{U_w}{f_w D}$ is not required in this study. $V_{R,onset}^{CF}$ is the reduced velocity from which the significant cross-flow VIV amplitude (0.15*D*) appears.

$\Psi_{proxi,onset} = \begin{cases} \frac{1}{5}\left(4 + 1.25\frac{G}{D}\right) & \frac{G}{D} < 0.8 \\ 1 & \text{else} \end{cases}$ is a correction factor accounting for the seabed proximity and is chosen as 1 in this case due to *G/D*=2.0. $\Psi_{trench,onset}$ represents the

correction factor accounting for the effect of a pipeline located in/over the trench and is chosen as 1 as well.

To sum up, $V_{R,onset}^{CF}=3$, $V_{R,1}^{CF}=6.4$, $V_{R,2}^{CF}=9.8$, $V_{R,end}^{CF}=16$ and $\left(\frac{A_{Z,1}}{D}\right)=\left(\frac{A_{Z,2}}{D}\right)=1.15$ in this case. The safety factor is chosen to be 1.3 for design and 1.0 for prediction respectively. Other cross-flow VIV amplitudes at different reduced velocities can be interpolated from Figure 24.

Figure 25 gives the comparison between numerical simulation results using three different soil models and the DNV Response model which is derived based on available experimental laboratory test data and several full-scale tests. The amplitude of vibration in cross-flow direction versus different reduced velocities is shown in the figure. A general agreement is observed. When the reduced velocity is small (less than 4) or large (greater than 12), all the three model results agree with the DNV Response model. When the reduced velocity ranges from 6 to 10 where the maximum amplitude occurs, the simulation results of three soil models are slightly different. The results of linear soil model are smaller than what the DNV Response model predicts. Results of soil model of Aubeny et al. (2006) are greater than those of linear soil model by about 10% and fit the DNV Response model well.

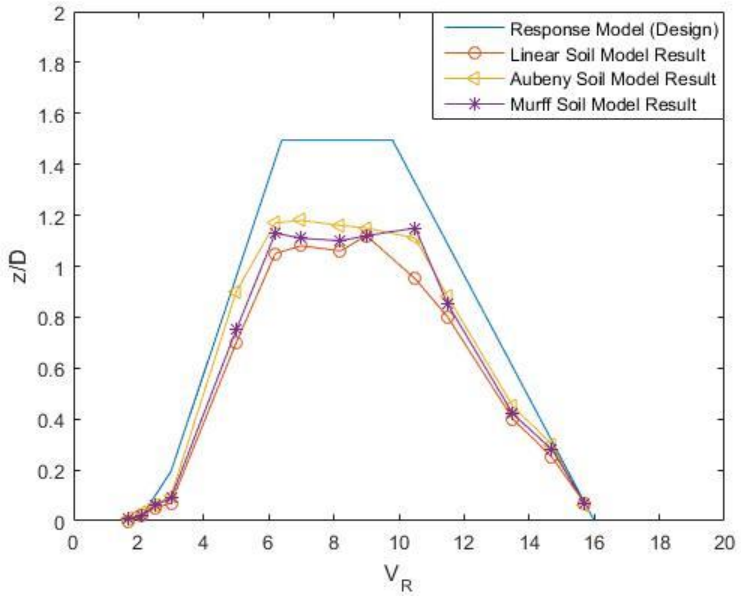

(a)

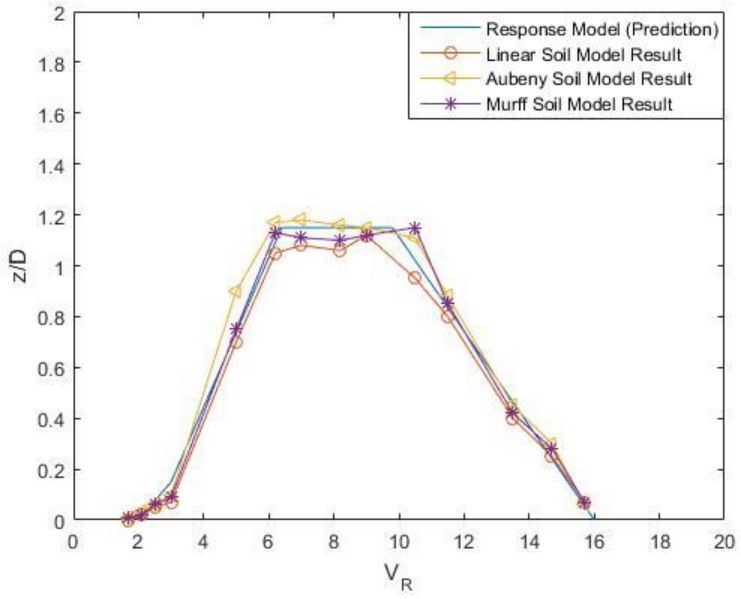

(b)

Figure 25 Comparison between Numerical Simulation Results and DNV Response Model (a) Safety Factor =1.3 (b) Safety Factor =1.0

The vibration amplitudes at different reduced velocities from the above numerical test cases are listed in Table 7. The soil type is chosen to be soft clay.

Table 7 Vibration Amplitudes at Different Reduced Velocities

Reduced Velocity	Linear	Aubeny	Murff
1.7	0	0.01	0.01
2.1	0.02	0.03	0.02
2.5	0.05	0.06	0.06
3.0	0.07	0.10	0.09
5.0	0.70	0.91	0.75
6.2	1.02	1.14	1.13
7.1	1.05	1.15	1.08
8.2	1.03	1.13	1.07
8.9	1.09	1.12	1.09
10.5	0.95	1.11	1.15
11.5	0.82	0.88	0.85
13.5	0.39	0.45	0.42
14.7	0.25	0.30	0.28
15.7	0.07	0.06	0.07

The vibration time histories applying Aubeny's soil model at different reduced velocity zones are shown in Figure 26. The reduced velocities are chosen to be 2.5, 8.2 and 14.7 for 'low reduced velocity zone', 'lock-in zone' and 'high reduced velocity zone' respectively. It is noted that the vibration amplitudes in the lock-in zone are relatively large because the vibration frequency coincides with the pipeline natural frequency.

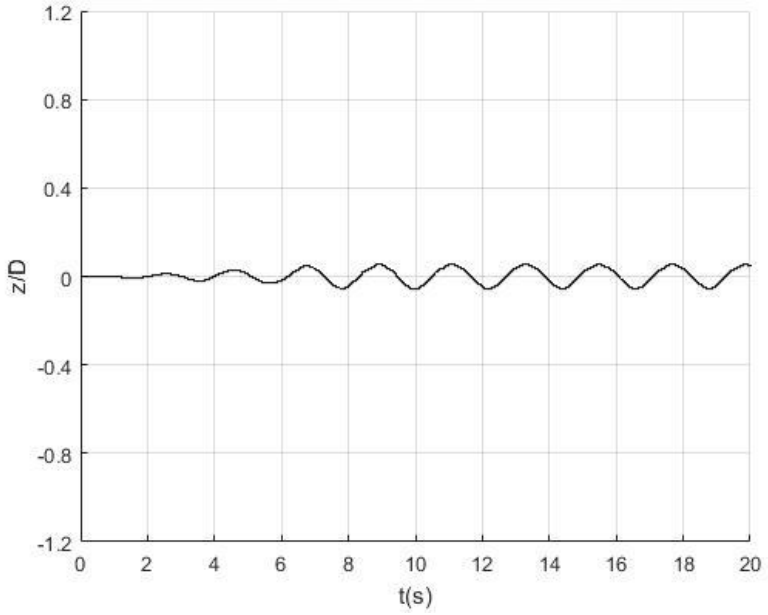

(a)

Figure 26 Vibration Time Histories at Different Reduced Velocity Zones (a) Low Reduced Velocity (b) Lock-in (c) High Reduced Velocity

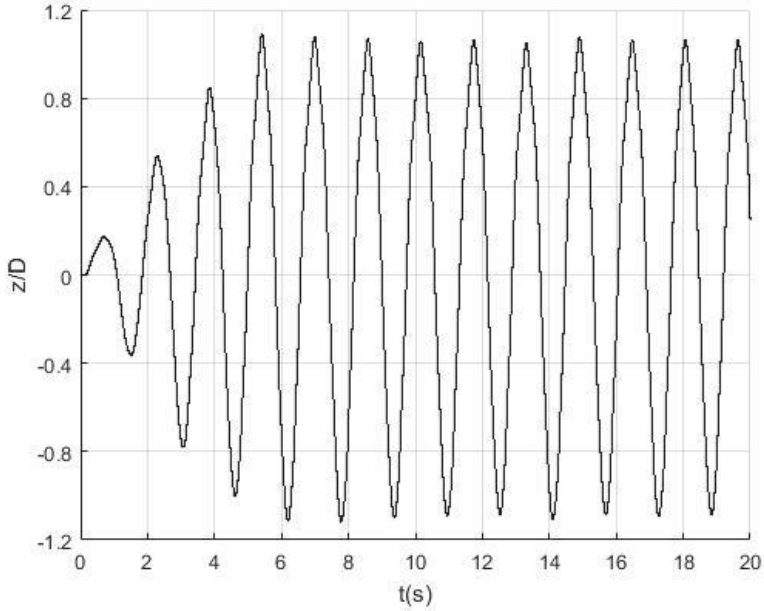

(b)

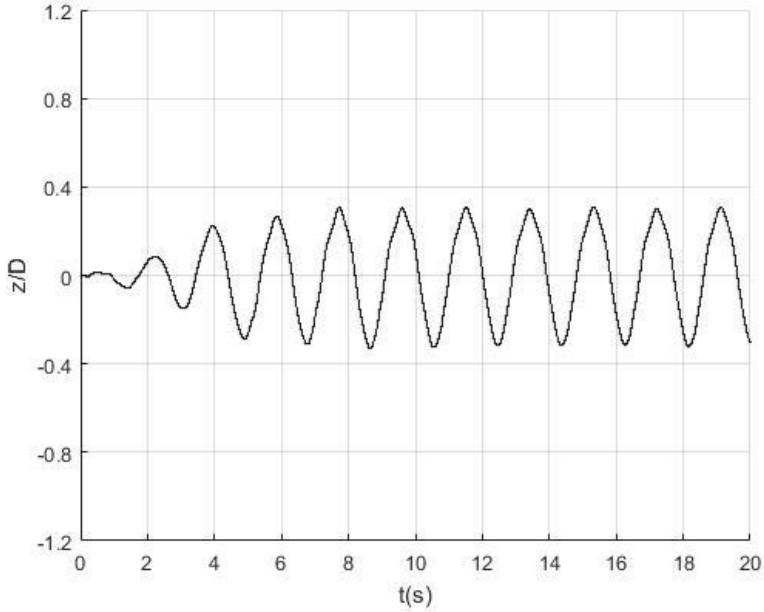

(c)

Figure 26 Continued

CHAPTER IV

COMPARISON BETWEEN GAP TO DIAMETER RATIOS

In previous VIV simulations of pipelines, near plane boundary effects were studied by several researchers. Angrilli et al. (1982) revealed that the near plane pipeline VIV frequency will decrease correspondingly as the gap to diameter ratio *G/D* increases. Pontaza et al. (2010) noticed that no classic vortex shedding were observed within the range $0.0< G/D <0.3$. In general, gap to diameter ratio is the main parameter which affects vortex shedding of the near plane pipelines. Thus, effects of gap to diameter ratio in the simulation of free span pipelines deserve to be studied due to previous researches of near plane pipelines. In this Chapter, we consider a free span pipeline of *L/D*=250 and *Ls/D*=150 lay in the sea bottom soil. The gap to diameter ratio *G/D* ranges from 1.2 to 3.0. Other parameters about the pipeline are listed in Table 8.

Table 8 Parameters of a Free Span Pipeline of Different *G/D*

Parameter	Value
Total Length *L*	5.0 m
Outer Diameter *D*	20.0 mm
Bending Stiffness *EI*	135.4 Nm^2
Weight Per Unit Length *W*	6.857 N/m
Pretention *T*	400 N

Grid Generation

Before CFD calculation, a new grid needs to be generated for this special case. We still use 6 blocks to cover the whole fluid field in this case. The gap to diameter ratio is set to be *G/D*=1.2, 1.8, 2.4, 3.0 respectively. Figure 26 depicts the fluid field middle section near view of *G/D*=1.2 and 3.0. The near body block (red) consists of 194012 (26×182×41) grid points; the wake block (green) consists of 149526 (26×81×71) grid points; the background block (blue) consists of 296946 (26×141×81) grid points; the top near wall block (black) consists of 76986 (26×141×21) grid points; the gap block (yellow) consists of 47376 (16×141×21) grid points; the bottom near wall grid (black) consists of 33840 (16×141×15) grid points. Thus, there are 798686 (about 0.8 million) computational nodes in total.

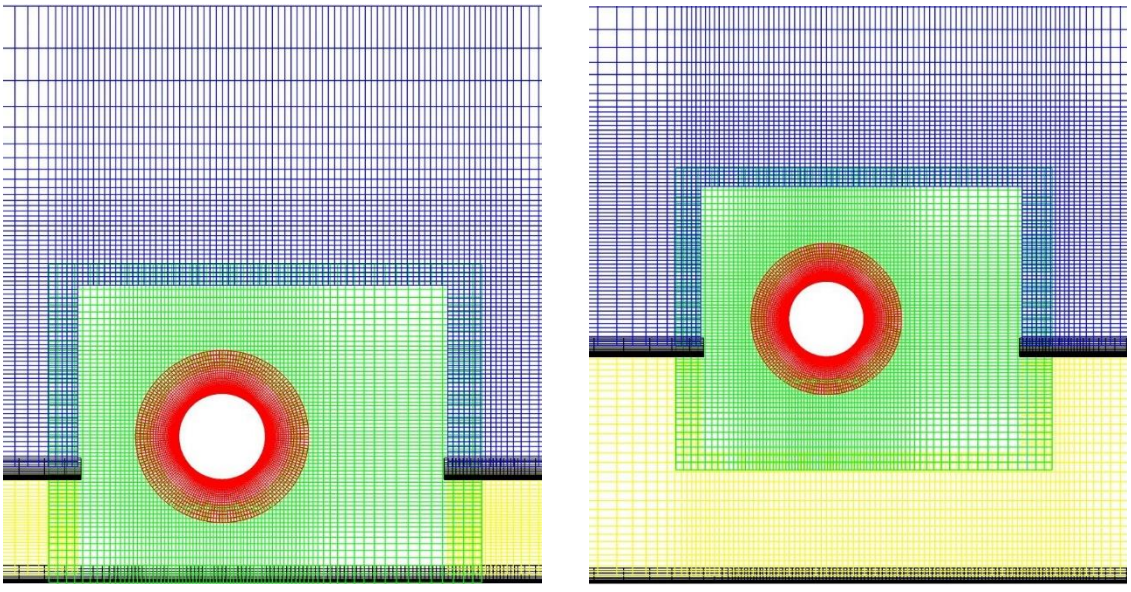

Figure 27 Middle Section Near View of *G/D*=1.2 and 3.0

Simulation Results

In the numerical simulation, the pipeline is exposed to uniform current of 0.4m/s. A medium sand type soil and the nonlinear soil model of Aubeny et al. (2006) is selected for the simulation. Figure 27 shows typical vorticity snapshots of the pipeline middle section of *G/D*=1.2~3.0. For the larger gap depth, we can see that the effect of bottom plane boundary is relatively small and the vortex shedding in a typical 2S pattern. For the smaller gap depth, the vortex generated by the bottom plane boundary cancels the vortex (in pink color) shed from the pipeline.

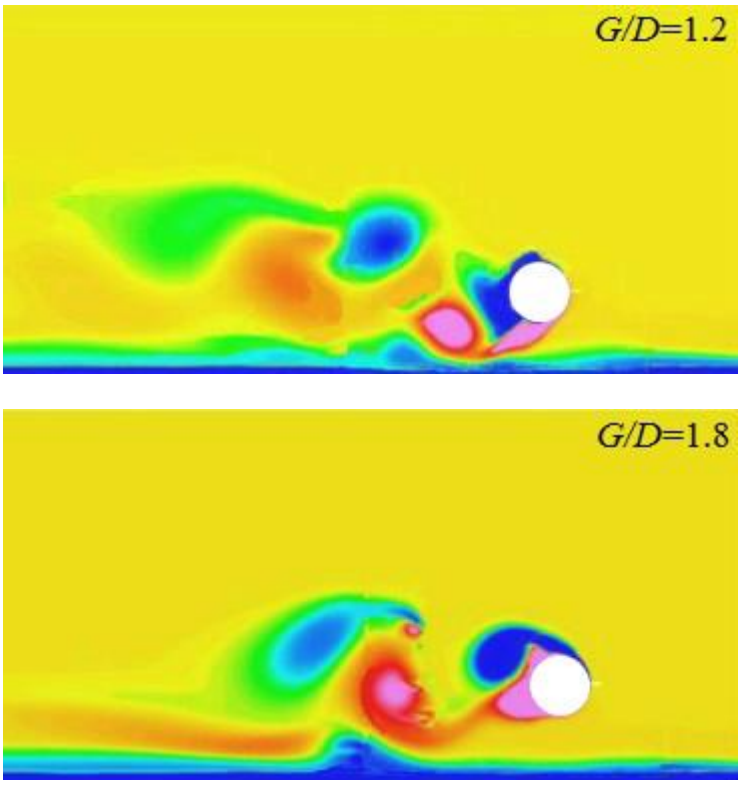

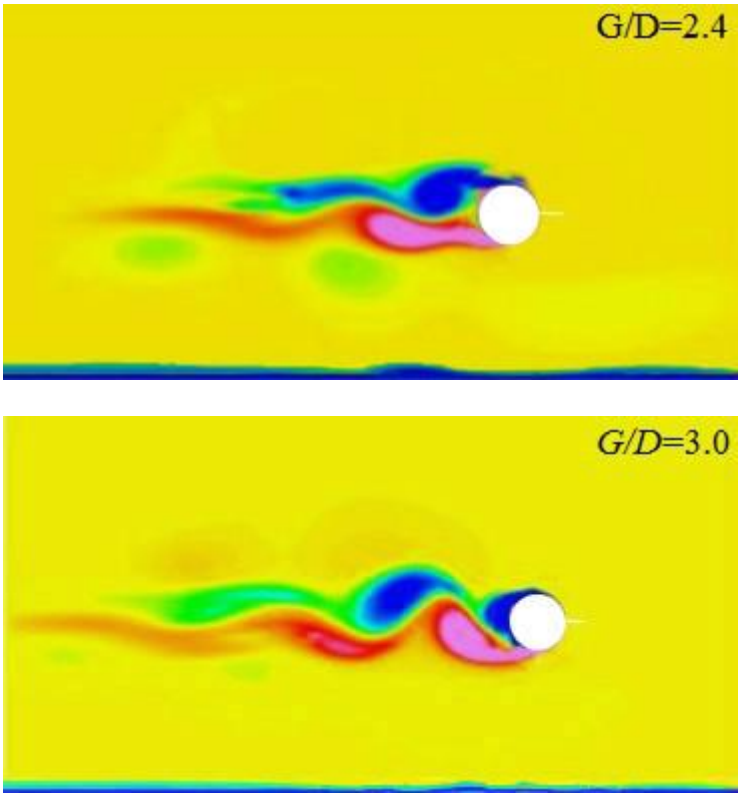

Figure 28 Typical Vorticity Snapshots of *G/D*=1.2~3.0

The cross-flow vibration time histories of the pipeline middle point with different gap to diameter ratios are plotted in Figure 28-31. The maximum vibration amplitudes are marked in the figures. For *G/D*=1.2, the maximum positive amplitude is *z/D*=0.8152 while the maximum negative amplitude is *z/D*=-0.6914. For *G/D*=1.8, the maximum positive amplitude is *z/D*=0.9027 while the maximum negative amplitude is *z/D*=-0.7833. For *G/D*=2.4, the maximum amplitudes are *z/D*=0.9518 and -0.8640 respectively. What is noteworthy is that the vibration amplitude is not symmetric about its original position when the gap to diameter ratio is relatively small. This may be explained by the pipeline proximity to the sea bottom soil: the compressed fluid in the gap would reduce the pipeline vibration amplitude. For *G/D*=3.0, the maximum

vibration amplitudes are *z/D*=1.0329 and -1.0536 which become approximately symmetric about the original position.

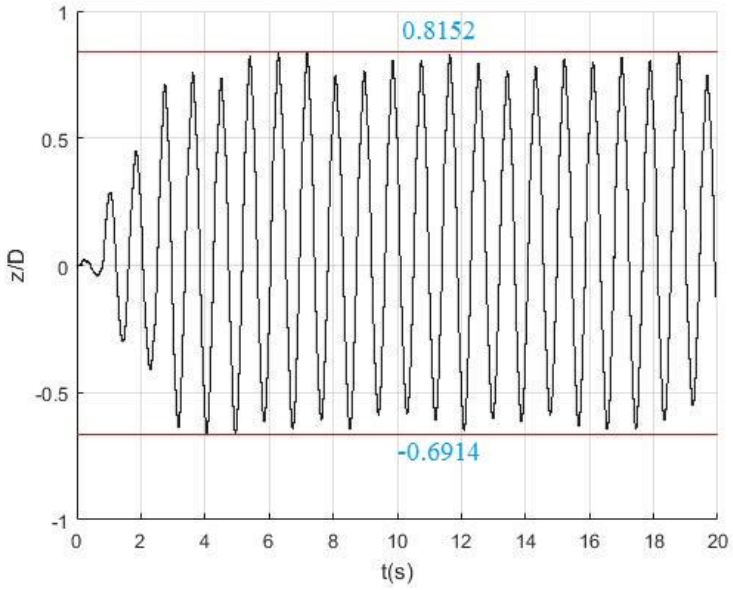

Figure 29 Cross-Flow Vibration History for *G/D*=1.2

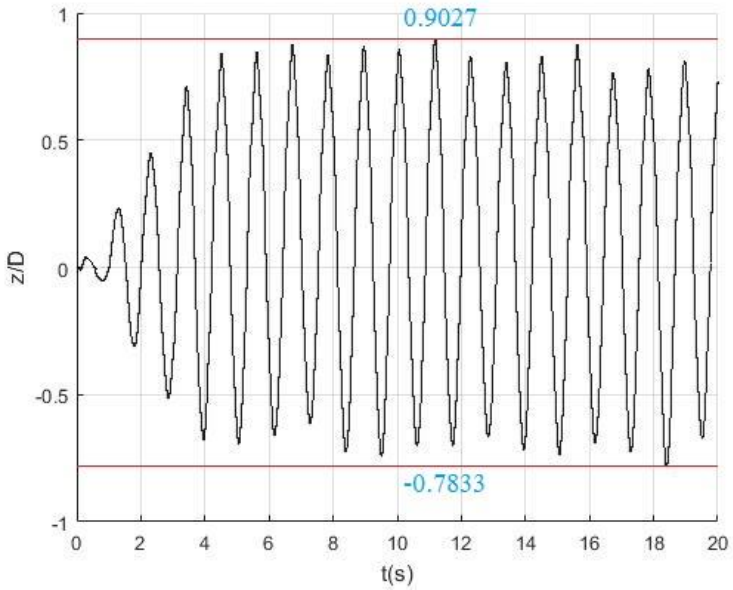

Figure 30 Cross-Flow Vibration History for *G/D*=1.8

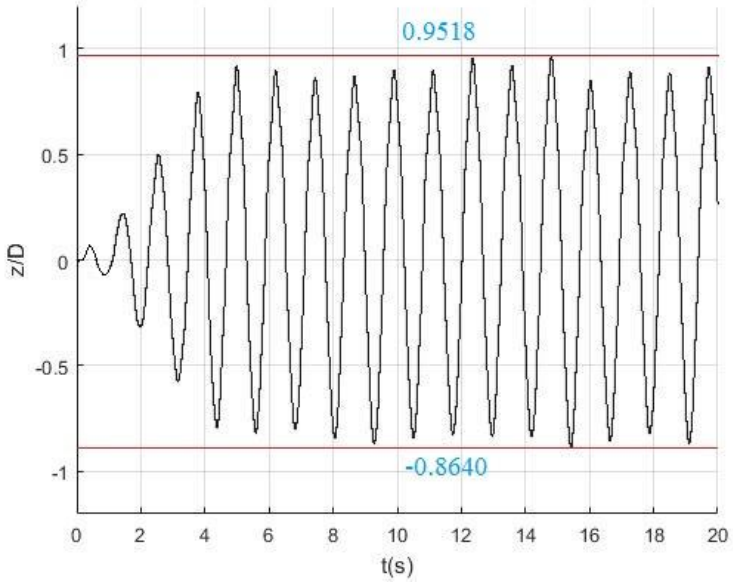

Figure 31 Cross-Flow Vibration History for *G/D*=2.4

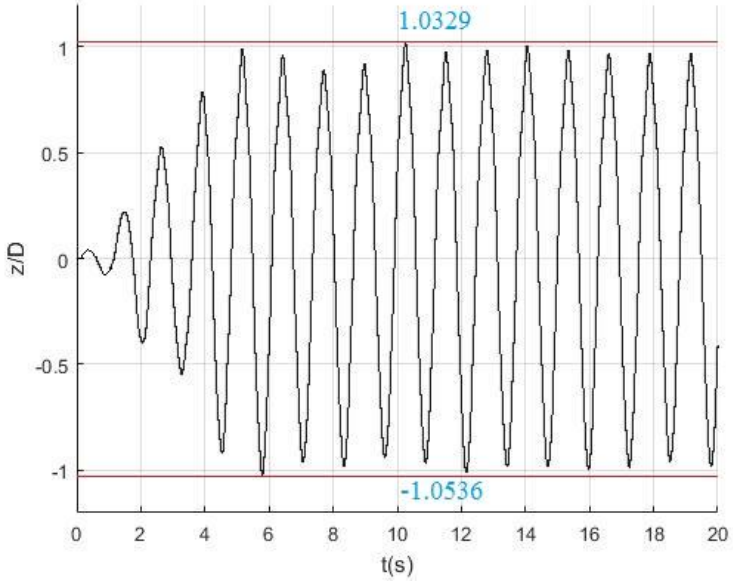

Figure 32 Cross-Flow Vibration History for *G/D*=3.0

The simulation results also reveal the relationship between VIV amplitude and gap to diameter ratio *G/D*. We take root mean square (RMS) of the vibration amplitudes to represent the mean value. As shown in Figure 32, the vibration amplitude will increase as *G/D* increases.

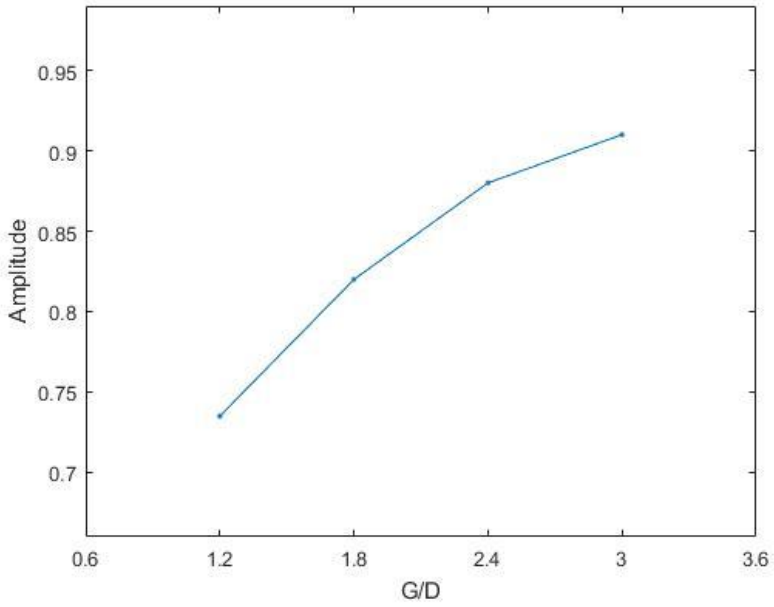

Figure 33 RMS Amplitude versus *G/D*

To figure out the relationship between VIV frequency and gap to diameter ratio *G/D*, Fast Fourier Transform (FFT) is applied to the vibration time histories. Take the result after FFT of vibration time history for *G/D*=1.2 as an example. From Figure 33, we can see that the cross-flow vibration frequency for *G/D*=1.2 is 1.12 Hz. Figure 34 shows that the VIV frequency increases significantly as *G/D* decreases.

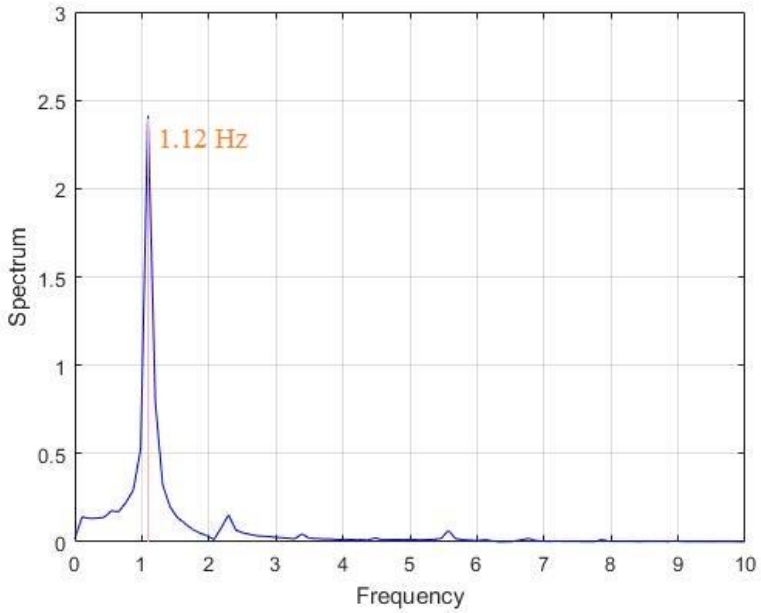

Figure 34 Fast Fourier Transform Result

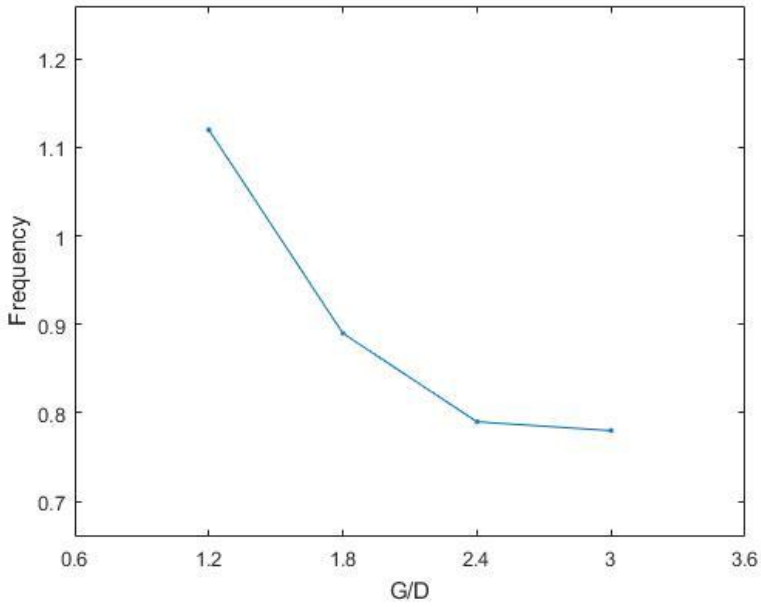

Figure 35 Frequency versus *G/D*

CHAPTER V

SUMMARY AND CONCLUSIONS

In this thesis, vortex-induced vibrations of free span pipelines have been investigated in numerical simulations including CFD and FSI. A pipeline motion solver with governing equations of a tensioned beam was developed and coupled with a three dimensional fluid solver to simulate fluid-structure interactions. A linear and two nonlinear soil models were included and compared in the pipe-soil interactions. In addition, overset grid and dynamic grid techniques were used in this study to avoid the time-consuming grid regeneration process.

First, a comparison between the linear soil model and two nonlinear soil models were conducted in both sand and clay type soil. Two points, the soil point which is at the edge of soil and the middle span point, were selected to show the cross-flow vibration time histories. The vibration amplitude at soil point using linear soil model is different from those using nonlinear when the penetration depth is relatively small or large. The vibration amplitude at span point using linear soil model is asymmetric about its original position.

Then, the numerical simulation results of the VIV amplitudes at different reduced velocities were validated using the Response Model provided by DNV-RP-F105 (2006). The safety factor was selected to be 1.3 and the simulation results using all three soil models agree well with the recommended practice. When the reduced velocity ranges

from 6 to 10 where the maximum amplitude occurs, the simulation results of three soil models are slightly different.

Finally, the effect of gap to diameter ratio on VIV amplitudes of free span pipelines were studied. The simulation results revealed the relationship between VIV amplitude and gap to diameter ratio: the vibration amplitude will increase as *G/D* increases. Asymmetric vibration amplitudes have been detected for pipeline VIV at relative small *G/D*. By applying Fast Fourier Transform (FFT) to the vibration time histories, it showed that the VIV frequency increases significantly as *G/D* decreases.

In conclusion, a 3D numerical approach consisting of motion solver, fluid solver and different soil models for solving deep water free span pipeline VIV problems has been presented. The effectiveness and validity of the numerical simulation were demonstrated by several case studies. The results have shed some light on the free span pipeline VIV problems.

REFERENCES

Aubeny, C. P., Biscontin, G., & Zhang, J. (2006). Seafloor interaction with steel catenary risers. Final Project Report to Minerals Management Service, Offshore Technology Research Centre Industry Consortium, Texas A&M University, College Station, Houston, TX, OTRC Library, (9/06A173).

Bridge, C., Laver, K., Clukey, E., & Evans, T. (2004, January). Steel catenary riser touchdown point vertical interaction models. In Offshore Technology Conference. Offshore Technology Conference.

Chen, H.C., & Patel, V.C. (1988). Near-Wall Turbulence Models for Complex Flows Including Separation. J AIAA, 26(6): 641-648.

Chen, H.C., & Patel, V.C. (1989). The Flow around Wing-Body Junctions. Symposium on Numerical and Physical Aspects of Aerodynamic Flows, 4th, Long Beach, CA. 1989: 1989.

Chen, H.C., Patel, V.C., & Ju, S. (1990). Solutions of Reynolds-Averaged Navier-Stokes Equations for Three-Dimensional Incompressible Flows. J Computational Physics, 88(2): 305-336.

Chen, H.C., Chen, C.R., & Huang, K. (2013). CFD Simulation of Vortex-Induced and Wake-Induced Vibrations of Dual Vertical Risers. Proc 23rd International Offshore and Polar Engineering Conference, Anchorage, Alaska, ISOPE.

Constantinides, Y., & Oakley, O. H. (2006, January). Numerical prediction of bare and straked cylinder VIV. In 25th International Conference on Offshore Mechanics and Arctic Engineering (pp. 745-753). American Society of Mechanical Engineers.

Dunlap, W., Bhohanala, R., & Morris, D. (1990). Burial of vertically loaded offshore pipelines. 22nd Annual Offshore Technology Conference, number OTC 6375, Houston, Texas. 263–270.

Fyrileiv, O., Mork, K., & Chezhian, M. (2005, January). Experiences using DNV-RP-F105 in assessment of free spanning pipelines. In ASME 2005 24th International Conference on Offshore Mechanics and Arctic Engineering (pp. 571-578). American Society of Mechanical Engineers.

Gamino, M., Abankwa, S., & Pascali, R. (2013, June). FSI methodology for analyzing VIV on subsea piping components with practical boundary conditions. In ASME 2013 32nd international conference on ocean, offshore and arctic engineering (pp. V007T08A028-V007T08A028). American Society of Mechanical Engineers.

Huang, K., Chen, H. C., & Chen, C. R. (2012). Vertical riser VIV simulation in sheared current. International Journal of Offshore and Polar Engineering, 22(02).

Wilde J. J. & Huijsmans, R. H. (2004, January). Laboratory investigation of long riser VIV response. In The Fourteenth International Offshore and Polar Engineering Conference. International Society of Offshore and Polar Engineers.

Meakin, R. L. (1999). Composite overset structured grids. Handbook of Grid Generation, 1-20.

Meneghini, J. R., Saltara, F., Andrade Fregonesi, R., Yamamoto, C. T., Casaprima, E., & Ferrari, J. A. (2004). Numerical simulations of VIV on long flexible cylinders immersed in complex flow fields. European Journal of Mechanics-B/Fluids, 23(1), 51-63.

Murff, J. D., Wagner, D. A., & Randolph, M. F. (1989). Pipe penetration in cohesive soil. Geotechnique 39, No. 2, 213-229.

Pantazopoulos, M. S. (1994). Vortex-induced vibration parameters: critical review (No. CONF-940230--). American Society of Mechanical Engineers, New York, NY (United States).

Petersson, N. A. (1999). Hole-cutting for three-dimensional overlapping grids. SIAM Journal on Scientific Computing, 21(2), 646-665.

Pontaza, J. P., Menon, R., Swanson, R., Jhingran, V., Hill, M., Kopp, F., & Hoffman, J. (2010, January). Fluid-Structure interaction simulations of a pipeline span exposed to sea bottom currents. In Offshore Technology Conference. Offshore Technology Conference.

Theti, R. (2001). Soil interaction effects on simple-catenary riser response. Pipes & pipelines international, 46(3), 15-24.

Tognarelli, M. A., Taggart, S., & Campbell, M. (2008, January). Actual VIV fatigue response of full scale drilling risers: with and without suppression devices. In ASME 2008 27th International Conference on Offshore Mechanics and Arctic Engineering (pp. 513-525). American Society of Mechanical Engineers.

Triantafyllou, M., Triantafyllou, G., Tein, Y. S., & Ambrose, B. D. (1999, January). Pragmatic riser VIV analysis. In Offshore technology conference. Offshore Technology Conference.

Tsukada, R. I., & Morooka, C. K. (2013, June). A Numerical Simulation Procedure for Vortex-Induced Vibration of Pipelines with Free Span. In ASME 2013 32nd International Conference on Ocean, Offshore and Arctic Engineering (pp. V007T08A057-V007T08A057). American Society of Mechanical Engineers.

Suhs, N.E. & Tramel, R.W. (1991). PEGSUS 4.0 User's Manual. Arnold Eng Dev Center Report AEDC-TR-91-8, Arnold Air Force Station, TN.

Veritas, D. N. (2006). Free spanning pipelines. Recommended practice DNV-RPF105.

Xiao, F. (2015). CFD Simulation of Vortex–Induced Vibrations of Free Span Pipelines Including Pipe-Soil Interactions. (Master's dissertation, Texas A&M University).

You, J. H. (2007). Numerical model for steel catenary riser on seafloor support (Doctoral dissertation, Texas A&M University).